NRC Form 390A | **U.S. NUCLEAR REGULATORY COMMISSION**
(12-2003)
NRCMD 3.9

RELEASE TO PUBLISH UNCLASSIFIED NRC CONTRACTOR SPEECHES, PAPERS, AND JOURNAL ARTICLES

(Please type or print)

1. TITLE (State in full as it appears on the speech, paper, or journal article)
Deformation Characteristics and Gas Permeability of Reworked Tuffaceous Sedimentary Rock Near Bishop, California: Implications for Later Flow

2. AUTHOR(s)
C. Dinwiddie, K. Bradbury, R. McGinnis, D. Ferrill, & R. Fedors

3. NAME OF CONFERENCE, LOCATION, AND DATE(s)
N/AVadose Zone Journal

4. NAME OF PUBLICATION
Soil Science Society of America

5. NAME AND ADDRESS OF THE PUBLISHER Soil Science Society of America, 677 South Segoe Rd, Madison, WI 53711	**TELEPHONE NUMBER OF THE PUBLISHER** (608) 273-6080 (Voice) (608) 273-2021 (Fax)
6. CONTRACTOR NAME AND COMPLETE MAILING ADDRESS *(Include ZIP code)* Southwest Research Institute Center for Nuclear Waste Regulatory Analyses 6220 Culebra Road San Antonio, Texas 78228 Attn: Cynthia Dinwiddie (Division 20)	**TELEPHONE NUMBER OF THE CONTRACTOR** (210) 522-6085

7. CERTIFICATION

(ANSWER ALL QUESTIONS)

	X	A. COPYRIGHTED MATERIAL	–	Does this speech, paper, or journal article contain copyrighted material? If yes, attach a letter of release from the source that holds the copyright.
	X	B. PATENT CLEARANCE –		Does this speech, paper, or journal article require patent clearance? If yes, the NRC Patent Counsel must signify clearance by signing below.
		NRC PATENT COUNSEL *(Type or Print Name)*	SIGNATURE	DATE
X		C. REFERENCE AVAILABILITY	–	Is all material referenced in this speech, paper, or journal article available to the public either through a public library, the Government Printing Office, the National Technical Information Service, or the NRC Public Document Room? If no, list below the specific availability of each referenced document.
		SPECIFIC AVAILABILITY		
	X	D. METRIC UNIT CONVERSION	–	Does this speech, paper, or journal article contain measurement and weight values? If yes, all must be converted to the International System of Units, followed by the English units in brackets, pursuant to the NRC Policy Statement implementing the Omnibus Trade and Competitiveness Act of 1988, Executive Order 12770, July 25, 1991.

8. AUTHORIZATION

The signatures of the NRC project manager and the contractor official certify that the NRC contractor speech, paper, or journal article is authorized by NRC, that it has undergone appropriate peer review for technical content and for material that might compromise commercial proprietary rights, and that it does not contain classified, sensitive unclassified, or nonpublic information. (NRC MD 3.9, Part II(A)(1)(d))

A. CONTRACTOR AUTHORIZING OFFICIAL *(Type or print name)* Robert Lenhard	SIGNATURE	DATE 8/30/2006
B. NRC RESPONSIBLE PROJECT MANAGER *(Type or print name)*	OFFICE/DIVISION	MAIL STOP

TELEPHONE NUMBER	E-MAIL I.D.	Did you place the speech, paper, or journal article in ADAMS? YES ☐ NO ☐ If so, provide the ADAMS Accession No. (Use Template OCIO 099) ______

SIGNATURE	DATE

Deformation Characteristics and Gas Permeability of Reworked Tuffaceous Sedimentary Rock Near Bishop, California: Implications for Lateral Flow

Cynthia L. Dinwiddie,* Kelly Keighley Bradbury, Ronald N. McGinnis,
David A. Ferrill, and Randall W. Fedors

C.L. Dinwiddie, R.N. McGinnis, and D.A. Ferrill, Dept. of Earth, Material, and Planetary Sciences, Geosciences and Engineering Division of Southwest Research Institute, 6220 Culebra Road, San Antonio, TX 78238; K.K. Bradbury, Utah Faults, Fractures, and Fluids (UF^3), Innovation Campus, Utah State University, 1770 Research Park Way, Ste. 183, North Logan, UT 84341; R.W. Fedors, U.S. Nuclear Regulatory Commission. *Corresponding author (cdinwiddie@swri.org). Received xxx 2006. Revised xxx 200x. Accepted for Publication xxx 200x. Original Research Paper.

ABSTRACT

Detailed lithological, structural, and in-situ permeability data were obtained within a fractured and faulted sequence of thinly bedded, poorly consolidated, reworked tuffaceous sedimentary rock and interbedded ashfall deposits near Bishop, California. This study characterizes the lithology of two beds within the unit and quantifies and assesses lithology-dependent, deformation-induced heterogeneities associated with small-displacement normal faults cutting across the bedded rock. This work is important because the poorly consolidated volcaniclastic deposits we studied serve as natural analogs to faulted and fractured bedded tuff units of the Paintbrush and Calico Hills nonwelded hydrogeologic units—units that are located stratigraphically above and below a potential high-level radioactive waste repository host horizon in Yucca Mountain, Nevada. Some workers have hypothesized that these types of units could potentially divert downward flow through the repository horizon, thus limiting the availability of water to corrode emplacement containers and dissolve and transport radioactive materials. Features identified in this analog study that may influence the distance over which water may be laterally diverted in the nonwelded bedded tuffs at Yucca Mountain include (i) hydrologic anisotropy imposed by steeply dipping faults; (ii) bed thickness, and ash, glass, and clay content of individual beds cut by small-displacement faults influence deformation zone widths and deformation styles; (iii) fault deformation zones in bedded tuffs can be locally wider than vertical fault displacement is long; and (iv) irregularly distributed fracture densities related to fault deformation may work in concert with pervasive vertical fractures to increase the hydrologic heterogeneity and permeability of the units they cut. (250 words)

Keywords: *Unsaturated Zone · Fractured Rocks · Heterogeneity · Arid Regions · Waste Disposal*

We present structural, petrophysical, and hydrogeological data obtained during characterization studies of reworked tuffaceous sedimentary rock and interbedded ashfall deposits as analog data for properties of bedded tuffs of the Paintbrush nonwelded hydrogeologic unit (PTn) at Yucca Mountain, Nevada. Studies related to this work and conducted near Bishop, California, include Ferrill et al. (2000), Fedors et al. (2001), Evans and Bradbury (2004), Dinwiddie et al. (2006), and McGinnis et al. (in revision for J. of Structural Geology). Our studies are motivated by the need to develop an appropriate conceptual model for fluid flow in the faulted and fractured PTn. We characterize deformation features associated with a small-displacement, horst-bounding fault and related subsidiary faults that cut across thinly bedded and poorly lithified tuffaceous units and examine lithological variations at the micrometer to meter scale. Degree of cementation, postdepositional crystallization, potential fluid-rock interactions, grain-size distribution, clay content, and the distribution of fracture systems are assessed for their influence on permeability heterogeneity.

Observations of structural deformation features over a wide range of scales provide the basis for understanding the effects of secondarily induced lithological changes on in-situ permeability architecture within unconsolidated to poorly consolidated deposits. This multidisciplinary research effort is unique because relatively little work has been performed to study the influence of brittle deformation on hydrologic properties in poorly lithified volcaniclastic strata (cf., Ferrill et al., 2000; Wilson et al., 2003; Evans and Bradbury, 2004; Dinwiddie et al., 2006). Results of this analog study may provide insight into the relationship between lithology-dependent deformation processes and the permeability architecture within bedded tuff units of the PTn that have similar physical properties.

Most deformation features impart secondary permeability characteristics onto the fabric of the undeformed protolith. Deformation features that form in poorly lithified porous rocks (e.g., deformation bands and faults) generally have zones of decreased pore size and reduced permeability with respect to the undeformed host rock (e.g., Antonellini and Aydin, 1994). These zones may result from pore collapse in deformation bands (Wilson et al., 2003), clay smear (Yielding et al., 1997), and cataclastic grain-size reduction (Heynekamp et al., 1999). Although small-scale, permeability-reducing deformation features that cluster near larger faults may locally decrease permeability by creating barriers to flow (Antonellini and Aydin, 1994; Odling et al., 2004), these same features may enhance flow within the surrounding material. The evolution of deformation mechanisms while strain accumulates within a fault zone can cause a complex pattern of permeability structure, especially within heterogeneous sediments.

Motivation, Background, and Objectives

This study was motivated by a need to reduce uncertainty regarding the potential length scale for lateral flow diversion within bedded tuffs of the PTn at Yucca Mountain, Nevada (Wu et al., 2002; Fedors et al., 2002; Flint et al., 2003). Nonwelded tuff and tuffaceous sedimentary rock units at Yucca Mountain, the site of a potential high-level radioactive waste repository, play important roles in deep percolation through the unsaturated zone in the PTn above the repository horizon and within bedded tuffs and reworked tuffaceous sedimentary rock of the Calico Hills Formation and Crater Flat Group below the repository host horizon. Yucca Mountain, an east-dipping cuesta associated with primarily west-dipping normal faults (Morris et al., 2004), is cut by numerous block-bounding and intrablock normal faults with meters to several hundreds of meters of displacement (Day et al., 1998a,b; Levy et al., 1999; Ferrill et al., 1999a; Ferrill and Morris, 2001; Morris et al., 2004).

The gently dipping PTn overlies the potential repository horizon and consists of several nonwelded units, including the vitric zone at the base of the Tiva Canyon Tuff, the pre-Tiva Canyon Tuff bedded tuffs, the Yucca Mountain Tuff, the pre-Yucca Mountain Tuff, the pre-Pah Canyon Tuff bedded tuffs, the Pah Canyon Tuff, and the vitric zone at the top of the Topopah Spring Tuff (Moyer et al., 1996) (Table 1 and Figure 1a). The PTn is often assumed to spatially and temporally dampen episodic pulses of meteoric infiltration percolating downward through the overlying Tiva Canyon welded unit. Dual permeability numerical simulations (Bechtel SAIC Company, LLC, 2004) suggest that a porous, permeable nonwelded tuff matrix may attenuate rapid, transient fracture flow from the Tiva Canyon welded unit; hence, a steady-state assumption is often made for unsaturated flow through the fractured tuffs of the potential repository horizon within the Topopah Spring welded unit (e.g., Bechtel SAIC Company, LLC, 2004) that is located below the PTn. Modeling by Wu et al. (2002; cf., Bechtel SAIC Company, LLC, 2004) suggested that large-scale lateral flow (~500 m) may occur down-dip along bedding planes in the PTn, thereby influencing the distribution of the percolation flux to the underlying repository horizon (Bechtel SAIC Company, LLC, 2003). Large-scale lateral flow could reduce the amount of water that percolates toward waste emplacement drifts by shedding water away from the drifts (Fedors et al., 2002; Fedors and Ferrill, 2002). The quantity and chemistry of water entering these drifts is important to corrosion of the waste containers, and dissolution and transport of the radioactive materials they contain. While some lateral flow is likely, it is important to estimate a realistic, physically based length scale for this phenomenon. Past length scale estimates vary from tens of meters (cf., Fedors et al., 2002; Flint et al., 2003) to kilometers (cf., Bechtel SAIC Company, LLC, 2004). From our perspective, primary heterogeneity combined with secondary discontinuities associated with small-displacement faults (not typically modeled) and their associated fracture networks may inhibit large-scale lateral flow within the PTn by focusing vertical flow into the underlying Topopah Spring welded tuff (e.g., Fedors et al., 2002; Dinwiddie et al., 2006).

Table 1. Rock properties of the PTn† and natural analog sites.

Unit	Lithologic Characteristics	Porosity	Density (g/cm^3)	k (m^2)‡
	PTn			
Tiva Canyon Tuff (Tpcpv1)	Non- to moderately welded, vitric	0.13–0.55	1.02–1.94	1×10^{-13}
Pre-Tiva Canyon bedded tuff (Tpbt4)	Nonwelded pumicefall to pyroclastic flow; light gray, 90–95% pumice clasts; < 5.4 m thick for all subunits	0.31–0.56	0.99–1.52	1×10^{-13}
Yucca Mtn Tuff (Tpy)	Non- to moderately welded	0.04–0.44	1.39–1.78	3×10^{-14}
Pre-Yucca Mtn Tuff bedded tuff (Tpbt3)	Weathered pyroclastic flow to pyroclastic fall, ashfall, pumicefall, and locally reworked deposits; light brown to light gray, 40–85% pumice clasts; moderately to poorly sorted; < 52.5 m thick for all subunits	0.12–0.53	1.11–2.16	1×10^{-13}
Pah Canyon Tuff (Tpp)	Non- to moderately welded	0.40–0.61	0.88–1.34	1×10^{-13}
Pre-Pah Canyon Tuff bedded tuff (Tpbt2)	Pumicefall to locally reworked deposits; < 15.8 m thick for all subunits	0.30–0.60	0.90–2.38	5×10^{-12}
	NATURAL ANALOG SITES			
Crucifix Site	Bedded, fluvially reworked Glass Mtn. Rhyolite and interbedded ashfall deposits	0.29–0.70	0.76–1.77	3×10^{-13}
Chalk Cove Site¶	Nonwelded to sintered Bishop Tuff	0.20–0.45	1.30–1.60	1×10^{-13}

†Moyer et al. (1996)

‡1 darcy = 0.986923×10^{-12} m^2; permeability given in millidarcies from this point onward

¶Dinwiddie et al. (2006) and references therein

Below the Paintbrush Group, the Calico Hills Formation and underlying Crater Flat Group include pyroclastic flow units, ashfall deposits, bedded tuffs, and tuffaceous sandstone layers (Moyer and Geslin, 1995; Engstrom and Rautman, 1996; Rautman and Engstrom, 1996a,b).

Like the overlying units, the Calico Hills Formation and Crater Flat Group units dip eastward and are cut by the large (map scale) normal faults of Yucca Mountain (e.g., Day et al., 1998a). The Calico Hills Formation and Crater Flat Group are not as well characterized as the massive nonwelded ignimbrites and bedded tuff units of the PTn because of poorer outcrop exposure, fewer borehole penetrations, and lack of tunnel-scale mapping. Borehole core and logging data from Yucca Mountain systematic drilling program wells SD-7 (Rautman and Engstrom, 1996a), SD-9 (Engstrom and Rautman, 1996), and SD-12 (Rautman and Engstrom, 1996b) reveal that the Calico Hills Formation and Crater Flat Group consist of vitric to zeolitic nonwelded tuff units, reworked bedded tuff, and tuffaceous sandstone. These units are depositionally and lithologically similar, in terms of heterogeneity, composition, and emplacement mechanisms, to the reworked tuffaceous sedimentary rock studied herein, and to the nonwelded to sintered Bishop Tuff studied by Dinwiddie et al. (2006). These core data also indicate that the Calico Hills Formation and Crater Flat Group are fractured and faulted with fault displacements ranging from centimeters to tens of meters. These faults (i) are steep to gently dipping, (ii) are brecciated in some cases, (iii) exhibit slickensides and oxidized iron staining, and (iv) exhibit a 6- to 7-cm-thick clay gouge in some cases. Coupled with the eastward dip, lithologic heterogeneity, diversity of fracture development, and range of fracture orientations, small-displacement faults in these units are expected to lead to a complex permeability architecture, similar to what we observed during analog studies of the basal Bishop Tuff (Dinwiddie et al., 2006) and during our studies of the underlying volcaniclastic deposits that we describe herein.

Unsaturated zone flow models populated with homogeneous interlayer property sets can predict lateral diversion of percolating water above layer interfaces that join two layers with strongly contrasting hydrologic properties (e.g., Wu et al., 2002; Bechtel SAIC Company, LLC, 2004). Permeability or capillary barriers to downward flow that are modeled in this way likely give rise to physically unrealistic estimates for the spatial scale of lateral diversion because primary heterogeneity and secondary heterogeneity induced by steeply dipping, small-displacement faults and associated fractures may significantly disrupt the lateral continuity of geologic interfaces (Dinwiddie et al., 2006). To evaluate the effect of primary lithologic heterogeneity and faults, fractures, and fault zone deformation on the hydrologic properties of reworked tuffaceous material as an analog to bedded tuffs of the PTn and to address the potential for disruption of lithologic barrier-induced lateral diversion of flow, we collected data from the Crucifix Fault, its deformed footwall block, and unfaulted rock deformed only by vertical fractures. Field and laboratory results from our study of two beds with different textures and grain sizes, which were influenced by this fault system, are presented to specifically address secondary deformation-induced heterogeneities and their potential effects on constraining the scale over which lateral flow diversion may occur.

The Analogy to Yucca Mountain

The analog study described here was performed with rocks (Figure 1b) similar to reworked deposits associated with bedded tuffs of the PTn (e.g., units Tpbt4, Tpbt3, and Tpbt2 of Table 1) at Yucca Mountain. Dinwiddie et al. (2006) previously presented analog data from the massive nonwelded ignimbrites of the PTn (e.g., units Tpcpv1, Tpy, and Tpp of Table 1). Poorly lithified clast- to matrix-supported tuffaceous sedimentary rock derived from the Glass Mountain volcanic complex is exposed in a cut bank along the Owens River near Bishop, California, and stratigraphically below the Bishop Tuff (Figure 1b). This exposure is informally named the Crucifix Site (cf., McGinnis et al., 2005). The reworked bedded tuffs of the PTn compare with the Glass Mountain-derived tuffaceous sedimentary rock at the Crucifix Site in the following ways:

- Both formations exhibit reworking of primary tephrafall and pyroclastic material. In particular, pre-Pah Canyon Tuff bedded tuff (Tpbt2) Unit D is cross-laminated tuffaceous pebbly sandstone, suggesting local fluvial reworking. Units B, C, and G of the pre-Yucca Mountain Tuff bedded tuff (Tpbt3) also exhibit reworking (Moyer et al., 1996; Figure 1a)
- Comparable units of the Glass Mountain-derived reworked sedimentary rock and the Paintbrush Group have similar porosities, bulk densities, and permeabilities (Table 1)
- Comparable units of the Glass Mountain-derived reworked sedimentary rock and the Paintbrush Group exhibit similar mineralogical and petrological characteristics [crystals (quartz and feldspars), lithic fragments, glass (shards and pumice clasts), matrix, iron oxides, alteration products, and grain size]
- Both formations have tectonic deformation histories characterized by extension, which was accommodated by normal faulting (Martel, 1989; Spengler et al., 1993; Dawers and Anders, 1995; Pinter, 1995; Ferrill et al., 1999a,b, 2000; Ferrill and Morris, 2001; McGinnis et al., 2005). Faults within these formations have similar geometries, associated deformation features, and effects on adjacent matrix material
- The number of steeply dipping, small displacement faults per meter (measured approximately parallel to bedding and perpendicular to fault strike) observed at the Crucifix Site is approximately double the number of small displacement faults per meter from detailed line survey data for analogous PTn units in the Exploratory Studies Facility (ESF) at Yucca Mountain (McGinnis et al., in revision). These small displacement faults

at Yucca Mountain strike approximately perpendicular to the PTn layer dip and, therefore, may influence or interrupt lateral flow paths in PTn layers.

The geometry and deformation features of a fault and their effect on adjacent matrix material are important to unsaturated zone flow in nonwelded bedded tuffs. The majority of faults exposed in the ESF at Yucca Mountain have < 3 m of displacement (Gray et al., 2005; CRWMS M&O, 1998). Twenty faults with < 4 m of displacement and steep dips were mapped in the north ramp of the ESF (Beason et al., 1996). The Crucifix Fault, as we will show, has a displacement on this scale. Faults at Yucca Mountain that cut through more than one hydrogeological unit have variable fracture intensity, trace length, and connectivity—properties that are dependent on the lithology of the host rock. In this paper we assess lithology-dependent deformation features. Faults with favorable orientations for slip or dilation are critical because they may be preferential fluid flow pathways (Ferrill et al., 1999b), and steeply dipping faults may constrain the scale of lateral flow. Short fracture tracelengths (< 1 m long) constitute a major component of the fracture network adjacent to fault zones at Yucca Mountain and are an important aspect of fault-related fracture systems (Hinds et al., 2003). In this paper, we assess the distribution and probable effects of short fracture tracelengths in faulted, bedded tuffaceous units.

LOCATION AND DESCRIPTION OF RESEARCH AREA

We examine and characterize poorly lithified, reworked, tuffaceous sedimentary rock exposed below the Bishop Tuff in northern Owens Valley near Bishop, California. Owens Valley is at the western edge of the Basin and Range physiographic province of North America and is nestled between the Sierra Nevada Mountains to the west and the White–Inyo Mountains to the east [cf., Figure 2 of Dinwiddie et al. (2006) and location description therein].

The Glass Mountain volcanic complex was a precursor to the Bishop Tuff eruption and represents the first magma erupted from the Long Valley magma chamber (Metz and Mahood, 1985). Glass Mountain eruptions occurred between 2.13 and 0.79 Ma, producing high-silica rhyolite lava deposits northeast of what is now the Long Valley Caldera (Metz and Mahood, 1985). Glass Mountain Rhyolite-derived material was transported by Pleistocene-age glacial meltwater in the form of debris flows, hyperconcentrated flood flows (Smith, 1986), and normal stream flows, redepositing tuffaceous sediments along the valley floor (Izett et al., 1988). This braided fluvial system flowed sporadically and was highly variable in its flow regime (McGinnis et al., in revision).

Erosion and structural uplift subsequently isolated these tuffaceous sedimentary deposits as a localized topographic high (McGinnis et al., in revision). The 0.76 Ma Bishop Tuff (Sarna-Wojcicki et al., 2000), which overlies these tuffaceous sedimentary rocks, formed as a nuée ardente-type pyroclastic flow (Gilbert, 1938; Wilson and Hildreth, 1997, 1998, 2003) and is significant to this study because the original thickness of the tuff sheet produced the maximum lithostatic stress on the tuffaceous sedimentary deposits (McGinnis et al., in revision), resulting in their partial lithification.

Where the Owens River emerges from the Owens River Gorge at the southern distal extent of the Bishop Tuff, the river turns sharply to the east across the Owens Valley, eroding the Bishop Tuff and forming an east-west exposure known locally as Chalk Bluff (Figure 2). The Crucifix Site is located toward the east end of the Chalk Bluff on Chalk Bluff Road (Figures 2 and 3a). In this location, the Bishop Tuff that once overlaid the Crucifix Site deposits is interpreted to have been eroded by the downcutting of the Owens River. River terrace deposits consisting of unconsolidated granite cobbles and gravel derived from the Sierra Nevada Mountains still remain above the exposure of reworked tuffaceous sedimentary rock (Figure 1b).

Previous Work

Lithology

The deposits at the Crucifix Site comprise pumiceous and ash-rich tuffaceous sedimentary rocks that exhibit varying degrees of fluvial reworking, consistent with a dominantly turbulent suspension stream system flowing into a slackwater basin or a shallow lake (B.E. Hill, personal communication, 2004). Interbedded in these units are a few thin ashfall deposits (W. Hildreth, personal communication, 2005), presumably erupted during a precaldera interval (pre-Bishop Tuff) 2.1 Ma to 790 ka. The exposure is 20 m thick, and the fluvially reworked ash and pumice beds are moderately to poorly sorted (Evans and Bradbury, 2004). This unit is characterized by 20- to 60-cm-thick poorly lithified consolidated and unconsolidated beds (Evans and Bradbury, 2004; Izett et al., 1988) that exhibit soft sediment deformation (including burrows, load casts, and root casts), paleosols, and channels (B. Hill, personal communication, 2004). The mineralogical and chemical compositions of the Crucifix Site beds are nearly identical to the Bishop Tuff pumicefall deposits (Izett et al., 1988) and are likely derived from reworking of the Glass Mountain Rhyolite deposit (B.E. Hill, personal communication, 2004; W. Hildreth, personal communication, 2005).

Tectonic History and Structural Setting

Deformation observed at the Crucifix Site is a product of east-west extension (McGinnis et al., in revision). The exposure trends WNW-to-ESE and ranges in height from < 1 m at each end to ~20 m near its center. Small-scale normal faulting and vertical and conjugate fracturing are preserved in this 110-m-long cut bank exposure of tuffaceous sedimentary rock (McGinnis et al., in revision; Ferrill et al., 2000). Faults have visible displacements of 1 mm to > 4 m and include east- and west-dipping faults that intersect and crosscut each other. This crossing conjugate style of faulting produces horst and graben features (Ferrill et al., 2000). Faults are absent from the majority of the exposure, but are concentrated in two zones at the western and eastern ends near two oppositely dipping, horst-bounding normal faults separated by 78.5 m (Figures 1b and 3b). These bounding faults correspond to the principal zones of maximum displacement with the highest fault frequencies occurring in the footwall of the western bounding fault (i.e., the Crucifix Fault; see Figure 3b).

McGinnis et al. (in revision) suggest two different hypotheses for the stress history under which the deformation structures at the Crucifix Site formed. First, vertical fractures may have been the primary deformation feature, and these original fractures were later overprinted by conjugate faults and fractures during maximum burial with additional vertical fractures being developed as the overburden decreased. Second (conversely), conjugate faults and fractures may have been the primary deformation features and were later overprinted by vertical (mode I) fractures as the overburden diminished to its current state.

STRUCTURAL AND HYDROGEOLOGICAL CHARACTERIZATION OF REWORKED TUFFACEOUS SEDIMENTARY ROCK AND INTERBEDDED ASHFALL DEPOSITS

Field and Laboratory Methods

We used an integrated lithologic and structural geologic characterization approach to provide a geologic context for in-situ gas permeability measurements of tuffaceous sedimentary rock at the Crucifix Site. Detailed outcrop mapping, grain size analysis, compositional and microstructural thin-section studies, specific gravity measurements, and X-Ray Diffraction

(XRD) analyses were conducted along two transects extending perpendicular from the western horst-bounding fault trace (hereafter the Crucifix Fault) eastward to 10.5 m into the footwall block (Figure 4). Permeability surveys and areal fracture density and fracture orientation surveys were conducted along two transects extending perpendicularly away from the Crucifix Fault eastward to 16.5 m into the footwall block.

Detailed data collection focused on two relatively well-consolidated beds (hereafter CF1 and CF2). These beds were selected for this study based on analogy with ashfall and reworked deposits in the bedded tuffs of the PTn (Figure 1a) and because of their lateral consistency in thickness and texture. Bed CF1 is white to light gray, averages 12.5 cm thick, and is interpreted to be either a primary ashfall deposit or a slackwater ashfall deposit because it is massive and exhibits no bedding (B. Hill, personal communication, 2004). Bed CF2 is greenish-gray to yellowish-greenish gray, averages 18.8 cm thick, and is interpreted to be a reworked pumiceous tephrafall deposit with possible development of a paleosol (B. Hill, personal communication, 2004). Data were also collected within the Crucifix Fault and from subsidiary fault zones.

Many of the methods employed at the Crucifix Site were described for a study of faulted nonwelded ignimbrite conducted by Dinwiddie et al. (2006). An abbreviated methods section follows, but the reader is referred to the previous study for detailed descriptions of the methodologies.

Geologic Mapping and Fracture Measurements

To assess stratigraphic and structural relationships within the reworked tuffaceous sedimentary rock and to correlate these relationships with locations where in-situ permeability data were collected, 1:25 scale outcrop mapping was completed within beds CF1 and CF2 in the footwall block of the Crucifix Fault (Figure 4). The Crucifix Fault trace represents the datum for detailed mapping; mapping extends east 10.5 m into the footwall block. Mapping at the centimeter scale highlights several of the features presented in an extensive fault and fracture survey of the exposure that was completed by McGinnis et al. (in revision).

Fracture orientation and trace length data from circular sample surveys performed around each drill hole by McGinnis et al. (in revision) include measurements of more than 3,000 fractures. Areal fracture densities (cm/cm^2) for vertical and conjugate fractures were determined by dividing total fracture trace length surrounding each permeability test hole by a 25-cm-diameter circular measurement area. Areal fracture density provides information regarding the intensity and distribution of fracturing throughout the exposure, but are not expected to wholly correlate with permeability data because of substantial differences in measurement location and averaging volume [fracture trace length was measured on the outcrop *surface* and sometimes above and below the lithologic beds of interest, whereas permeability was measured over a very localized volume with highly nonlinear weighting (cf., Dinwiddie, 2005) and approximately 10 cm *beyond the surface* of each bed].

Grain Size, Sorting, and Weight Percent Fines Analyses

Grain size samples were collected from exposed material at the proximal end of small permeability test holes that were drilled into Beds CF1 and CF2 and also from fault material intersecting these beds. Samples were collected for standard sieve analysis (cf., Boggs et al., 1995) to track centimeter-scale changes in lithologic properties throughout each bed, such as mean grain size, degree of sorting, and weight percent fines (cf., Dinwiddie et al., 2006). The grain size sampling survey for Bed CF1 extended eastward to 10.5 m with respect to the datum located at the Crucifix Fault trace. Thirty-seven grain size samples were collected in Bed CF1. The survey for Bed CF2 extended from 0 to 10.25 m, and 38 samples were collected from this bed. The total mass collected averaged 76 grams per sample for Bed CF1 and 112 grams per sample for Bed CF2, with the difference due primarily to Bed CF1 being generally thinner, more ash rich, and slightly more cohesive than Bed CF2.

Grain size samples were dry sieved and hand shaken to reduce disruption of the ash particles, to avoid abrasion of the pumice fragments by overshaking, and to include the low density pumice and glass shards fraction that might have otherwise separated out of the fines using liquid settling methods. Standard granulometry methods (e.g., Balsillie et al., 2002) were used to analyze grain size and formulate cumulative probability curves. Weight percent fines data were also calculated from the original grain size data. We selected a cutoff grain size of 0.0625 mm (or 4φ, where the grain size measure $\varphi = -\log_2[d/d_0]$ and $d_0 = 1$ mm) for the weight percent of fines of the total sample because this diameter represents the upper limit for ash deposits defined by Fisher (1961, 1966) for pyroclastic sequences. Thus, the weight percent of fines is a proxy for the ash contained in each sample.

Microstructural Analyses

Microstructural analyses were performed on thin sections using a standard transmitted-light petrographic microscope to evaluate textural and compositional characteristics of both samples deformed by faults and lithologic samples that are relatively undeformed. A few thin section samples were collected from beds CF1 and CF2, but most were collected from deformed rock, either from the main Crucifix Fault zone or from the footwall block. Seventeen samples impregnated with blue-stained epoxy were studied using standard optical petrography techniques, including some samples used for previous work by Evans and Bradbury (2004). Samples collected from deformed rock were examined to identify specific deformation mechanisms and deduce the potential influence of microstructural features on porosity and permeability.

Twelve thin sections (grain mounts) were analyzed for mineral composition using a modified point-count method. Individual counts were made every 0.5 mm to form a 150-point grid over the slide area. The composition was recorded at each point with subcategories designated for crystals and crystal fragments (quartz and feldspar), pumice and glassy fragments, lithics, fine-grained matrix, and alteration products that include iron oxides, carbonates, and zeolites (cf. Schmid, 1981; Boggs, 1992). Individual point counts were recorded as a percentage of the total count. To compare weight percent fines with thin-section point count data, we used the total percentage of fine-grained matrix as an analog to the weight percent fines.

Compositional Analyses

Very fine-grained particles and abundant glassy material within this reworked tuffaceous sedimentary rock make thin-section identification of minerals and fine-grained alteration products within the matrix difficult. Therefore, as a supplemental technique for determining whole rock composition, XRD analyses were also performed. Representative samples were collected within Beds CF1 and CF2 and from the main fault and subsidiary faults. Twenty-one powdered samples were mounted on standard dry glass slides and XRD analyses were performed at 2° step intervals from 2° to 60°. This work expands on previous compositional analyses of samples from the Crucifix Site that were conducted by Evans and Bradbury (2004).

Porosity and Density Analyses

Sample collection and specific gravity measurement techniques as described by Evans and Bradbury (2004, see their Appendix) were used to calculate porosity values. Samples were obtained from Beds CF1 and CF2 and from within the Crucifix Fault. A total of five lithologic samples (two from Bed CF1 and three from Bed CF2) and four fault zone samples were specifically tested to determine porosity for this study.

Small-Drillhole Minipermeameter Survey

A small-drillhole minipermeameter probe (Molz et al., 2002; Dinwiddie et al., 2003; Dinwiddie, 2005) was used to measure the gas permeability of tuffaceous sedimentary rock at the Crucifix Site. The same general approach was used by Dinwiddie et al. (2006) to assess permeability heterogeneity due to a fault system in the nonwelded Bishop Tuff (see Table 1, Chalk Cove Site). Use of this in-situ method (i) eliminates the need to extract fragile samples for laboratory analysis and (ii) minimizes effects of weathering on the measured permeability value by sampling rock that is not directly exposed to the atmosphere. The small-drillhole minipermeameter probe is inserted into a 10-cm-long, small-diameter hole until the faceplate contacts the conical end of the drill hole. An annular rubber tip seal undergoes axial compression, causing the seal to radially expand like a packer against the sides of the drill hole. The packer seals the probe to the distal end of the drill hole while isolating the injection zone through which pressurized nitrogen gas is introduced to the porous medium. Pressure within the sealed-off region is maintained above atmospheric, so that nitrogen gas enters the porous medium, flows around the tip seal, and exits to the rock surface at ambient pressure. After steady-state conditions are achieved, several pressure and flow-rate pairs are recorded.

Given an assumption of homogeneity within the averaging volume, the measured injection pressure, flow rate, and a numerically determined geometrical factor describing the flow system, the effective gas permeability of the porous medium surrounding the drill hole was calculated with a standard semianalytical inverse solution (Dinwiddie, 2005). The pressure transducer and three flow meters were each calibrated to NIST-traceable standards at the beginning and end of field campaigns. When necessary, calibration curves were used to correct pressure or flow rate data. A portable, homogeneous ceramic check source was also used to calibrate the small-drillhole minipermeameter system daily in the field. Pressure and flow rate data pairs from each location were analyzed for the presence of high-velocity flow effects, and corrections were made if warranted. In the arid, windy outcrop environment of the Crucifix Site, water saturation is naturally low; thus, the use of effective gas permeability data as a surrogate for intrinsic permeability is thought to be appropriate (i.e., the relative permeability for a gas is approximately unity).

The complete permeability data set for the Crucifix Site was collected over a total of three separate field campaigns. Initially, the permeability sampling intervals were approximately 0.5 m and the survey terminated at a distance of ~10.5 m from the Crucifix Fault, but measurement density was ultimately increased to a sampling interval of approximately 0.25 m and the survey line was extended to a distance of 16.5 m. Data are particularly sparse in the first two meters of the footwall and near the conjugate faults (Figure 4a) because these areas were subject to intense deformation that weakens the rock and hastens weathering processes, thereby limiting the number of measurements. Permeability test holes were drilled approximately perpendicular to the local outcrop face. Permeability was determined for (i) 67 locations in Bed CF1, including three fault locations, (ii) 76 locations in Bed CF2, including three fault locations, and (iii) four locations in the core gouge of the main Crucifix Fault core.

RESULTS

Geologic Mapping and Fracture Density

The Crucifix Fault is a north-south striking, west-dipping fault with a normal sense of offset and 3.77 m of displacement (McGinnis et al., in revision) and is characterized by a 20-cm-thick fault core gouge bounded by two discrete 1- to 3-mm-thick bounding slip surfaces coated with white calcite (Figure 5). The fault core thickness varies from 1.5 to 30 cm vertically (Evans and Bradbury, 2004). Cataclasis and shear smear or normal fault drag deformation processes contributed to a well-developed, fine-grained fault gouge surrounded by vertical layers of host rock material that were locally dragged up to 1 m and entrained within the heterogeneous fault core. The Crucifix Fault core is either filled with calcite, coated with clay, or consists of fine-grained comminuted gouge mixed with glass fragments or pumice clasts, depending upon location.

Deformation is pervasive throughout the Crucifix Fault footwall block exposed at the Crucifix Site (Figure 4), but little deformation is observed within the hanging wall (Evans and Bradbury, 2004; McGinnis et al., in revision). The footwall exhibits a nonuniformly faulted (i.e., 47 scanline-measured faults) and fractured region extending eastward approximately 10 m. Of those 47 mapped faults, 25 fault traces were observed within a 2-m-wide zone immediately east of the Crucifix Fault trace. The footwall block is characterized by small-displacement antithetic, synthetic, and en echelon faults (Evans and Bradbury, 2004). Beds adjacent to these smaller faults are offset by numerous centimeter-scale slip surfaces. Mineralization surfaces up to several milimeters thick composed of calcite or silica are observed along some of these smaller slip surfaces (Evans and Bradbury, 2004). Associated fractures are typically open, 1–5 mm thick, and vertical to steeply east or west dipping. The hanging wall, however, has no associated faults and only centimeter-scale subvertical fractures immediately west of the fault (cf., McGinnis et al., in revision).

The geometry of individual faults at the Crucifix Site is dependent on the scale of displacement and the grain size of the beds through which the faults cut (McGinnis et al., in revision). Centimeter- and subcentimeter-scale displacement faults at the Crucifix Site contain distinct slip surfaces, but have no discernible core or damage zone [i.e., similar to Class A faults observed at Yucca Mountain (cf., Gray et al., 2005)]. Decimeter-scale displacement faults have distinct slip surfaces and a small fault core and damage zone. Cataclasis (cf., Engelder, 1974) and postdepositional mineralization are observed along the fracture planes of some of these faults [i.e., similar to Class C faults observed at Yucca Mountain (cf., Gray et al., 2005)]. The western horst-bounding Crucifix Fault exhibits features consistent with all three architectural components of the Caine et al. (1996) model—a measurable central fault core with slip surfaces, a distinct damage zone, and an undeformed protolith (Evans and Bradbury, 2004; McGinnis et al., 2005) [i.e., similar to Class D faults observed at Yucca Mountain (cf., Gray, et al., 2005)]. The fault cores are composed of fine-grained comminuted material; local thicknesses are dependent on the grain size of the bed encountered by the fault. Coarse-grained beds produce a locally thicker fault core and fine-grained beds produce a locally thinner fault core. Strain hardening that occurs in coarse-grained beds may result in thicker fault cores, while strain softening that occurs in fine-grained beds may yield thinner fault cores or slip surfaces (McGinnis et al., in revision). In either case, the intrinsic permeability of a fault core is expected to be small as a result of (i) grain comminution and pore collapse in coarse-grained material and (ii) clay smear processes in fine-grained material.

The photomosaic of Figure 4a clearly illustrates the intensity of deformation within the layered and poorly consolidated deposits at the Crucifix Site. A complex pattern related to deformation along the steeply dipping main faults produces a high intensity of subparallel and anastomosing fault and fracture surfaces with both intersecting systematic fracture sets adjacent to the main fault and nonsystematic intrablock fractures. The simplified lithostratigraphic map shown in Figure 4b highlights the structural architecture of the two lithologically distinct beds (CF1 and CF2) and locations where permeability, grain size, and fracture data were collected. Prominent fault systems with offsets ranging from 2 cm to several meters and with fault core thicknesses ranging from <1 cm to 30 cm are shown on the map. A summary of lithologic properties for Beds CF1, CF2, and fault systems is provided in Table 2.

Table 2. Rock properties of Crucifix Site deposits and fault elements.

Unit/Feature Identifier	Unit/Feature Description†	Lithologic Characteristics
CF1	Upper bed	• White to light gray, ash-rich fallout deposit, either a primary or slackwater deposit • Density: 0.92 g/cm^3 • Porosity: 0.63 • Thinly bedded (12.5 cm average thickness) • Poorly sorted • Average composition: 21.8 wt% crystals (quartz, feldspar); 0.7 wt% lithics; 13.3 wt% glassy fragments and pumice; 59.8 wt% fine-grained matrix; 4.4 wt% miscellaneous‡ • Grain size: 78 wt% fines (≤ 0.0625 mm) on average; geometric mean grain size: 0.15 mm
CF2	Lower bed	• Greenish-gray to yellowish-greenish gray, reworked pumiceous tephrafall deposit • Density: 1.21 g/cm^3 • Porosity: 0.52 • Thinly bedded (18.8 cm average thickness) • Moderately to poorly sorted • Average composition: 32.0 wt% crystals (quartz, feldspar); 10.0 wt% lithics; 20.0 wt% glassy fragments and pumice; 36.7 wt% fine-grained matrix; 1.3 wt% miscellaneous‡ • Grain size: 19 wt% fines (≤ 0.0625 mm) on average; geometric mean grain size: 0.40 mm
CF3a	Crucifix Fault core	• Fault core gouge composed of variable layers of entrained bedding and clay • Density: 0.76–1.77 g/cm^3 • Porosity: 0.29–0.70 • Average composition: 11.3 wt% crystals (quartz, feldspar); 2.4 wt% lithics; 13.6 wt% glassy fragments and pumice; 69.9 wt% fine-grained matrix; 2.8 wt% miscellaneous‡ • Grain size: 51 wt% fines (≤ 0.0625 mm)
CF3b	Subsidiary faults	• Average composition: 20.3 wt% crystals (quartz, feldspar); 1.7 wt% lithics; 26.0 wt% glassy fragments and pumice; 51.3 wt% fine-grained matrix; 0.7 wt% miscellaneous‡ • Grain size: 58 wt% fines (≤ 0.0625 mm)

†See Figure 4 for location

‡Iron oxides and alteration products

Two distinctive fracture patterns were observed in the exposure—a vertical fracture set and two sets of oppositely dipping steep but nonvertical (conjugate) fractures (also cf., Evans and Bradbury, 2004; McGinnis et al, in revision). Of the fractures mapped at the Crucifix Site, 74 percent are vertical and a response to tensile stress and the remainder are nonvertical and a response to shear stress. Vertical fractures are dominant in nonfaulted areas of the exposure, whereas nonvertical fractures are dominant in highly faulted areas. The two primary conjugate sets of fracture orientations include a northeast-striking, steeply south dipping set oblique to the Crucifix Fault and a southwest-west striking, steeply northwest dipping set parallel to the Crucifix Fault. Vertical fractures are consistently present, although not uniformly developed, throughout the exposure (Figure 6). Conjugate fracturing varies, however, as a function of distance away from the Crucifix Fault and into the footwall block (Figure 6). The greatest concentration of conjugate fractures occurs (i) in a highly faulted section between the Crucifix Fault at 0 m and 10 m into the footwall and (ii) in a nonfaulted section located 14.5 to 16.5 m east of the Crucifix Fault. These data also show that intense fracturing associated with meter-scale faulting extends into the footwall block for approximately 6 m with minor variation dependent on the bed lithology, and beyond this distance, conjugate fracturing tapers off significantly. Fracture intensity (Figure 4b) decreases with distance from the main Crucifix Fault trace, and the footwall block has more pervasive fracturing than does the hanging wall block.

Grain Size, Sorting, and Weight Percent Fines

Grain size data provide information about depositional and deformational processes at the centimeter scale. The data are highly skewed toward smaller grain sizes (Figure 7a); therefore, the geometric mean is the appropriate measure of central tendency for this parameter. On average, the primary or slackwater deposited ashfall material of Bed CF1 has a 0.15 mm grain size, while the reworked pumiceous tephra material of Bed CF2 has a 0.40 mm grain size. Excursions from average behavior that tend to occur at similar distances from the western bounding fault are attributed to a combination of the random occurrence of large pumice clasts and the potentially nonrandom occurrence of more agglutinated particles near the Crucifix Fault.

That particles in this location remained strongly agglutinated upon handshaking and sieving (a method selected to preserve delicate volcaniclastics) indicates cementation is perhaps related to fluid flow of a mineralized water. Average standard deviation values for both beds indicate the deposits are poorly sorted, with Bed CF1 being more poorly sorted than Bed CF2, as is expected when comparing a primary deposit with a reworked (homogenized) deposit.

A measure of the weight percent fines was calculated for each sample as a proxy for ash content or fault zone grain comminution (Figure 7c). As expected, weight percent fines decrease with increasing mean grain size (Figure 7d). The fines or ash content of Bed CF1 is 78 percent, and the fines or ash content of Bed CF2 is 19 percent (Table 2), consistent with their interpreted lithology. The weight percent fines within the fault rocks (Table 2, CF3a and CF3b) represent the percentage of fine-grained material (clay-size fraction) that is, to some extent, a result of cataclasis and associated grain comminution during slip along the fault (see Table 2).

Petrophysical Observations

Thin-section analyses, XRD techniques, and specific gravity measurements were used to characterize the tuffaceous sedimentary rock at the Crucifix Site. Glass (shards and pumice fragments), quartz, feldspars, and sanidine are the primary constituents of all outcrop samples (Table 2), with minor amounts of lithic fragments (predominately pumice) and alteration products. Amorphous silica and iron oxides are the primary fillings and coatings along fracture surfaces, with calcite coatings observed locally along the main Crucifix Fault and subsidiary faults. The modal content of thin sections, based on petrological point-count observations, are given in Table 3. Because many units at the Crucifix Site are reworked and our efforts are focused on the hydrologic properties of these materials, the mineralogical or textural subdivision of this geologic material (Table 3) was modified from the standard classification schemes for pyroclastic deposits and fragments (%crystals, %glass, and %lithics) as recommended by Schmid et al. (1981). The average composition of samples from Bed CF1 (e.g., Figure 8a) is 22 percent crystals, 13 percent glass or pumice, < 1 percent lithics, and 60 percent fine-grained matrix (ash and glass), whereas the average composition of samples from Bed CF2 (e.g., Figure 8b) is 32 percent crystals, 20 percent glass or pumice, 10 percent lithics, and 37 percent fine-grained matrix. These results are consistent with the weight percent fines determined for each bed through grain size analysis. Crucifix Fault zone samples comprise, on average, 11 percent crystals, 14 percent glass or pumice, 2 percent lithics, 70 percent fine-grained material, and 3 percent miscellaneous constituents, such as calcite. Slip surface samples from a small-displacement fault located at approximately 9.65 m along the transect (see Figure 4) comprise 20 percent crystals, 26 percent glass or pumice, 2 percent lithics, and 51 percent fine-grained matrix.

Table 3. Composition of Crucifix Site samples from point count thin section analysis.

Sample ID†	Unit/Feature Sampled	Crystals/ Crystal Fragments	Wt% Glass or Pumice	Wt% Lithics	Wt% Matrix (clay/ash mix)	Wt% Misc.‡
BT-68c	Fault gouge – above survey	25	16	3	51	5
BT-69	White ash bed *similar to* CF1	9	7	0	82	3
BT-90	Slip surface	21	33	3	42	1
BT-91	Slip surface	20	19	< 1	61	0
BT-92	CF2 host rock	32	20	10	37	1
BT-93	CF1 host rock	15	5	2	71	7
BT-104a	Fault gouge	1	21	0	77	0
BT-105	Fault gouge	0	3	0	95	3
BT-106	Fault gouge	41	29	0	27	3
BT-107a	Fault gouge	5	8	0	85	1
BT-107b	Fault gouge	<1	3	0	95	1
BT-107c	Fault gouge	23	22	1	51	3

†Refer to Figure 4 for sample collection location

‡e.g., iron oxide, calcite, zeolite, mica

Identifying minerals within the fine-grained material by point counting was difficult because of the unique texture imparted by the abundance of glass shards in the samples. X-Ray diffraction techniques were thus used to identify clays or other alteration products within the matrix material and fine-grained fault gouge. Quartz, amorphous silica, glass, feldspars, tridymite, cristobolite, and mica are the primary constituents of these rocks. The presence of quartz-tridymite-cristobolite-feldspar assemblages suggest some devitrification and alteration of glassy constituents in the sampled beds and more so within the fault zones (Vaniman et al., 2001; Bradbury and Evans, 2004). Minor to trace amounts of aluminosilicates, iron oxides, calcite, and amorphous aluminum hydroxides were also observed. Clay minerals identified in several samples include kaolinite and illite. Trace amounts of hydrated aluminosilicates and zeolites (analcime, clinoptilolite, laumontite) were found in a few samples and are likely the result of the initial stages of glass alteration.

Photomicrographs of textural and structural deformation elements (Figures 8–12) further convey their characteristics and potential influence on permeability architecture. Blue-dye epoxy was injected into the samples to impregnate pores and show microporosity in thin section. Material from Bed CF1, collected ~5.2 m east of the Crucifix Fault (as shown on Figure 4b), is comprised of delicate glass shards and quartz within a fine-grained glass- and clay-rich matrix (Figure 8a). Trace amounts of kaolinite and iron-oxide alteration is evident from XRD analysis. A felty texture is observed with magnification, which may indicate partial devitrification. Injection of blue epoxy into this sample shows that microfractures have the potential to control flow within this thin and porous ash layer. The blue epoxy did not impregnate (fully fill) the microfracture, but rather focused around the outer edges of the fracture, impregnating the surrounding matrix. Material from Bed CF2, collected ~9 m east of the Crucifix Fault (as shown on Figure 4b), shows a fiamma, or flame-shaped structure, which indicates the presence of a devitrified pumice clast (Figure 8b). Alteration of glass within this clast and the brownish hue of the matrix also suggest the initial stages of clay development. The dark brown coating around several individual grains indicates the formation of clay rims. Material composition is volcanic glass, quartz, feldspars, ash, and clay. Bed CF2 is coarser than Bed CF1 and contains less ash.

Photomicrographs of fault samples collected in the Crucifix Fault footwall block at ~9.65 m (as shown on Figure 4b) illustrate features and deformation mechanisms (Figure 9) that suggest a complex history of deformation—a history that should yield heterogeneous permeability architecture. For example, the development of overgrowth textures, thought to occur through diffusive mass transfer, is observed (Figure 9a). Overgrowth textures can locally reduce porosity. In the same thin section, however, dilation mechanisms are observed with blue epoxy filling pore spaces of both the matrix and a fracture. The presence of the clay mineral kaolinite (Figure 9b) suggests hydration and alteration of glass. Hydration is an important process because it may locally reduce porosity and permeability.

Microstructural deformation increases in samples nearer to the Crucifix Fault. A sample from a fault surface near the eastern conjugate fault [~4.9 m along the transect (Figure 4)] and in an intensely fractured region of the footwall damage zone shows intense iron-oxide staining and clay filling a fracture within the fault zone (Figure 10). Kaolinite and the zeolite analcime were detected with XRD. Hairline fractures oblique to the clay-filled fracture remain open. Grain rotation and comminuted material is observed as a result of cataclastic deformation mechanisms.

Several core samples from the main Crucifix Fault illustrate vertical and horizontal variations (Figures 11 and 12). Bounding slip surfaces transition to vertical layers of ash and sand, to mixed grain sizes, to a core that is composed of very fine-grained comminuted material intermixed with lithic fragments and convoluted clay gouge (Figure 12b). The fault gouge in the eastern-most layer in the fault core is coarser (Figure 11) than material in the center of the fault core. The central core exhibits the finest grain clay gouge and comminuted ash with single micrometer-scale fractures (Figure 12b). Abundant crystal and glass fragments are found near the edge of the fault core (Figure 11a). Mineralized and open fractures are found throughout the edges of the core, and some fractures exhibit both characteristics (Figures 11b and 12a). Partial mineralization may affect the overall porosity and permeability of fracture systems. Fractures also commonly splay into several microfractures near their tips (Figure 11b).

The presence of illite, kaolinite, amorphous silica (glass), quartz, sanidine, and trace zeolites is suggested by XRD analysis. Irregular geometry, distribution, and discoloration of the clay core and surrounding comminuted material (Figure 11c) are evidence that the fault core was a conduit for fluid flow during slip. Bleached halos of material surrounding clay gouge and the subsequent mineralization of hairline fractures suggest an evolution in fault zone behavior during its deformation that may be related to multiple phases of deformation and corresponding pulses of fluid flow. Upon cementation and cessation of faulting, fault core zones having abundant clay gouge would likely act as barriers to cross-fault fluid flow. Overall, the lithological and petrophysical properties of the fault core vary across-fault and along-fault at the micrometer scale.

Overall, the sampled Crucifix Site units are very porous (Table 2). Bed CF1 samples have an average specific gravity of 0.92 and a porosity of 63 percent. Bed CF2 samples have an average specific gravity of 1.21 and a porosity of 52 percent. Samples from the Crucifix Fault and subsidiary faults produce a wide spectrum of values, with specific gravities ranging from 0.76 to 1.77 and porosity ranging from 29 to 70 percent. Unweathered volcanic tuff and ash typically have porosity ranging from 14 to 50 percent; weathering can increase these values to more than 60 percent (Fetter, 1994), and unconsolidated deposits of silt and clay exhibit porosities ranging from 35 to 50 percent (Davis, 1969). Our calculated porosities are comparable to those reported in the literature for partially reworked bedded tuffs of the PTn at Yucca Mountain (Table 1).

Permeability

The permeability data for both lithologic beds are highly skewed toward lower values (Figure 13); therefore, the geometric mean is the appropriate measure of central tendency for this parameter. On average, the primary or slackwater deposited ashfall material of Bed CF1 exhibits a larger permeability value (342 md) than the more homogeneous reworked pumiceous tephra material of Bed CF2 (254 md). The two populations exhibit essentially the same level of variability (coefficient of variation for each bed is 1.20), and they both exhibit the presence of erratically large values (coefficient of variation > 1) at similar distances from the Crucifix Fault (Figure 13), suggesting that secondary heterogeneities in both beds are attributable to some combination of shear and tensile deformation overprinting between 0 and 10.5 m along the transects. Between 10.5 and 16.5 m, large permeability values (especially near 14 m along the transects; Figure 13) probably reflect the intersection of test holes with vertical fractures connected to the exposure surface.

Bed CF1 is more poorly sorted (more heterogeneous) with a smaller average grain size compared to Bed CF2, yet Bed CF1 is also slightly more permeable. This peculiarity may be attributed to sintering of grains, observed in thin sections, in what may be a primary ashfall deposit (Bed CF1). Sintering can lead to more brittle deformation and the development of more intense fracturing and microfracturing. The average permeability of the two lithologic beds, however, is not significantly different, given that this property can range 13 orders of magnitude in geological materials.

In comparison to data collected by Dinwiddie et al. (2006) for faulted nonwelded to sintered ignimbrite of the Bishop Tuff, the permeability distribution for rocks at the Crucifix Site is more heterogeneous. The host rock permeability for nonwelded ignimbrites of the Bishop Tuff averaged 120 millidarcies with a standard deviation of 5 millidarcies. Fault zone deformation in the sampled material generally increased the heterogeneity of the pyroclastic deposits at the Chalk Cove site by less than a factor of five, with all measurements being restricted to less than two orders of magnitude variation (Dinwiddie et al., 2006). One caveat to note is that the permeabilities of large-scale (i.e., ~20-m long) open fractures at the Chalk Cove site were not measured by the minipermeametry method.

At the Crucifix Site, however, the lithology of the host rock, the shear-stress deformation (conjugate faulting and fracturing), and the lithostatic stress deformation (vertical fracturing) combine to create permeability heterogeneities spanning more than three orders of magnitude; both smaller and larger values of permeability were measured here than were measured at the Chalk Cove site (Dinwiddie et al., 2006). Permeability ranges from 6 millidarcies to nearly 4 darcies in Bed CF1, and from 15 millidarcies to more than 3 darcies in Bed CF2. The crumbling, weathered nature of the bedded units near the Crucifix Fault and the crossing conjugate faults led to fewer permeability measurements in these areas of great interest. Intense fault deformation in these locations weakened the rock and almost certainly leads to higher matrix permeability in areas adjacent to slip surfaces. Sparse data collected within various layers of the core of the Crucifix Fault (see Figure 5a) varied by just less than an order of magnitude. Unlike the work that was presented by Dinwiddie et al. (2006), we did not measure the primary permeability of undeformed host rock at the Crucifix Site per se because even portions of the outcrop that do not exhibit shear deformation do exhibit tensile deformation, which influences the secondary permeability of the measured volume. The deformation history of the Crucifix Site, thus, prevents the efficacious determination of *host rock* or *background* primary permeability.

We do not develop a formula herein that relates permeability architecture at the Crucifix Site directly to grain size information and areal fracture density because the poor sorting exhibited by the sampled units and their fracture deformation prohibits using simple $k = Cd^2$ formulations, and because crossplots of permeability with areal fracture density (Figure 14) reveal a general absence of direct correlation between these measured properties. We reiterate here that it is more informative to observe general trends in areal fracture density and permeability throughout the sampled exposure (Figures 6 and 13) than to look for direct correlations because of differences in the size of averaging volumes employed by the different techniques and because permeability was sampled 10 cm below the exposed rock while fracture trace lengths were measured at the exposure surface and over an area defined by a 25-cm-diameter circle that generally partially extends above and below the individual bed thicknesses that are of interest. The discussion that follows is, therefore, limited to observations that can be supported by the suite of data collected at the Crucifix Site.

DISCUSSION

Lithological and Structural Controls that Influence Permeability

Field description of the Crucifix Site illustrates the asymmetrical geometry around the main slip plane of the Crucifix Fault as follows: (i) the Crucifix Fault core composition varies both vertically and horizontally along the length and width of the slip surfaces; (ii) the Crucifix Fault displacement, 3.77 m, is *less than* the width of its footwall deformation zone; (iii) the hanging wall deformation zone spans a few centimeters west of the fault trace, whereas the footwall deformation zone extends approximately 10 m; and (iv) the footwall deformation zone width varies between the two lithologically distinct beds [deformation features are present to ~6 m into the footwall for both Beds CF1 and CF2 but with slight variations (Figures 6), not including very narrow deformation zones in each bed that are associated with a small fault located at ~9.65 m along the transect].

Deformation characteristics also differ between Beds CF1 and CF2. Bed CF1 is dragged further into the Crucifix Fault zone than Bed CF2, probably because Bed CF1 has more ash and fines and is a thinner bed, which may facilitate its ductile movement into the most intense areas of deformation. In less deformed areas, Bed CF1 demonstrates a brittle style of deformation with numerous tight, short tracelength, hairline fractures that appear coated or mineralized in a thin section (Figure 11a). Bed CF1 may indeed be a primary ashfall deposit rather than a slackwater deposit because we observe the effects of sintering at the microscopic level. Fine-grained material exhibits interlocking grain boundaries and has a fuzzy and indistinct quality when magnified. In an undeformed unit, sintering will reduce porosity; however, in a deformed unit sintering-related embrittlement may result in increased numbers of microfractures that will increase its secondary permeability. Immediately adjacent to the Crucifix Fault, the coarser and *relatively* ash-poor Bed CF2 typically comprises the outer or mixed zones of the fault core. At increasing distances from the fault, Bed CF2 is characterized by open dilatant fractures and wide but filled fractures mineralized with clay or iron oxides (Figures 11b, 12). Deformation style in an individual bed (Figures 4 and 6) is thus related to a number of properties that include grain size, weight percent fines, ash content, and bed thickness.

Our results are consistent with recent works by others (Caine, 2005; Rawling and Goodwin, 2003; Du Bernard et al., 2002), which have shown that in addition to brittle deformation mechanisms (such as cataclasis, dilation, and transgranular fracturing), poorly lithified siliciclastic sediments also exhibit distributed deformation and deformation by ductile micromechanisms. The distribution and textural characteristics of these deformation features may locally influence porosity and permeability variations within the two lithologically distinct beds at the Crucifix Site. For example, dilation bands (Du Bernard et al., 2002) are observed primarily within Bed CF2 (a reworked tephrafall deposit). Dilation bands locally increase porosity (observe blue epoxy highlighting a fracture surface in Figure 12a). In the Crucifix Fault core, porosity and permeability vary widely (Table 2–CF3a and Figure 5a) as a result of anastomosing zones of intensely deformed, very fine-grained material occurring adjacent to less deformed, poorly sorted material (Figure 12). Fault core thin sections (Figure 12) illustrate zones of cataclastic deformation and porosity reduction within a surrounding damage zone of dilatant microfracturing, similar to the results of Main et al. (2001).

The Crucifix Site is unique, however, when compared to recent studies of sandstones and other poorly consolidated deposits (Bense, 2005; Caine, 2005; Rawlings and Goodwin, 2003; Du Bernard et al., 2002) because its material composition includes abundant glassy fragments and ash. Physical analog modeling by Wolf et al. (2003) has shown that less strain is required to develop shear bands in glass beads than in sand, and that grain size and bed thickness can influence the spacing and overall shape of shear bands. Differences in deformation characteristics observed between Beds CF1 and CF2 may also be influenced by these bed-specific attributes. The fluvial deposition of units exposed at the Crucifix Site further contribute to a unique style of deformation that includes both brittle and ductile deformation features at the micrometer- to centimeter-scale.

Deformation observed at the Crucifix Site is thought to superimpose additional heterogeneities onto the primary permeabilities of the ashfall (Bed CF1) and reworked tephrafall (Bed CF2) units and thereby influence fluid flow (see Figures 6 and 13, and the locally higher values of permeability in both beds where faulting is intense between the Crucifix Fault and the crossing conjugate faults). A high density of conjugate fractures and small-displacement faults are clustered around relatively larger displacement faults at the Crucifix Site (Figures 4 and 6). Vertical fractures related to lithostatic stress (overburden) and conjugate fractures related to shear stress should create more permeable beds together than would be exhibited by undeformed host rock, although this cannot be objectively demonstrated given lack of information about the permeability of the beds before they were deformed. Cataclastic fault zone deformation involves grain cracking and grain crushing, and thereby, grain size and pore volume reduction that results in the development of low permeability fault gouge. Water flowing laterally above a capillary or permeability barrier in a gently sloping unit would be interrupted and focused downward if that unit had been locally dragged into the core of a small-displacement fault.

In the variably saturated vadose zone, the influence these localized low- and high-permeability elements have on water movement depends on saturation conditions. Under locally saturated conditions, cataclastic fault gouge will behave as a barrier, while open fractures will behave as conduits. Under unsaturated conditions, water may wick into and be retained in fine-grained fault gouge, open fractures may behave as capillary barriers that cause water to be retained within the smaller pores of adjacent host rock, and filled fractures may behave as permeability barriers that prevent cross-block flow (e.g., Fedors et al., 2002). The development and distribution patterns of fractures will also evolve with time. Microfractures may intermittently be open following their formation. Precipitation of carbonates, iron oxides, and clays, including zeolites, may later occlude these surfaces, and later still these surfaces may reopen as a function of the presiding stressfield because these minerals are structurally weak (Yanagimoto and Iijima, 2003).

Hydraulic anisotropy in siliciclastic fault zones is expected to result from clay-smearing, bed dragging, grain reorientation and vertical segmentation of the fault plane (mechanisms described by Bense, 2005)—we observed the end result of these mechanisms at the Crucifix Site. The presence of the Crucifix Fault and the associated crossing conjugate normal faults in the footwall block may create permeability anisotropy at the centimeter to meter scale (Evans and Bradbury, 2004; Ferrill et al., 2000). This type of fault system is expected to influence fluid flow both vertically and laterally. Vertical fluid movement should be focused down dip and lateral fluid movement should be restricted horizontally by faults behaving as flow barriers. Influences such as these would potentially enhance fluid flow in a direction parallel to the intersection line of conjugate faults (McGinnis et al., in revision).

Microscopic analyses indicate clay forms (i) as a function of diagenesis related to the alteration of glass and feldspars (Figure 9a) and (ii) as a result of ductile deformation along the faults (Figures 11c and 12b). The presence and distribution of clays within these beds and faults is important because recent work suggests that clay films may play a significant role in the mechanical behavior of fault zones (Schleicher et al., 2006).

The development of clays and discontinuous iron-oxide fillings, the weathering of feldspars to fine-grained clays, and some evidence of features that may form in fault zone material in association with fluidization (e.g., see Figure 12b), which were observed in samples from faults and intensely fractured regions, may suggest the presence of groundwater during deformation. The glass content of ash-rich layers or lenses may contribute to the brittle deformation style observed at the Crucifix Site. The abundant volcanic ash within the primary or slackwater-deposited ashfall and the reworked tephrafall deposits may have behaved as a lubricant when hydrated [similar to the behavior of fly ash as a concrete additive that initially assists with fluidization and ultimately enhances strength (Muhunthan et al., 2004; Copeland, 2003)], leading to fluidization of ash-rich material within these fault zones. As water left the system, the volcanic ash may have chemically reacted with calcium and oxides to produce a less permeable and a *relatively* more cohesive material. In summary, the ash content of individual bedded tuff units will likely affect the nature of small-scale deformation features associated with subvertical faults that cut through the bedded units.

Implications for the Expected Scale of Lateral Flow in the PTn at Yucca Mountain

PTn subunit contacts are not flat, and many subunits exhibit gradational contacts rather than sharp boundaries; however, these physical details that affect the scale of the lateral flow phenomenon are not easily modeled at the mountain scale. Models are typically constructed, therefore, using assumptions that stratigraphic contacts have smooth boundaries and exhibit sharp hydrologic property contrasts. Both of these assumptions promote lateral flow (Fedors et al., 2002; Flint et al., 2003). The photomosaic and lithostratigraphic map of bedded units at the Crucifix Site (Figure 4) illustrate the uneven nature of stratigraphic surfaces in beds that are continuous for 78 m (cf., McGinnis et al., in revision). The geometric mean permeabilities calculated for beds at the Crucifix Site do not exhibit sharp property contrasts between two lithologically distinct, mappable bedded units; rather, the hydrologic property contrasts within the individual beds are more remarkable (Figure 13). Unsaturated zone flow models of nonwelded ignimbrite and bedded tuff units at Yucca Mountain may thus overestimate the scale of lateral flow occurring above model layer interfaces that artificially function as flow barriers.

Modeling by Wu et al. (2002) led to their conclusion that the ptn23/ptn24 contact is a capillary barrier to vertically flowing water. This result is thought to be a modeling artifact because a gradational contact physically occurs at this massive ignimbrite to bedded tuff interface (Fedors et al., 2002; Fedors and Ferrill, 2002). The base of the bedded tuffs Tpbt4 and Tpbt2 are possible locations for permeability barriers to form (i.e., coarse-grained units overlying fine-grained units) (Fedors and Ferrill, 2002), but the base of units Tpbt4 and Tpbt2 do not coincide with the base of model layers (CRWMS M&O, 2000). The base of bedded tuff Tpbt3 is excluded as a potential capillary barrier based on an analysis of constitutive relationships for model layers ptn24 and ptn25, which follows in more detailed discussion.

Analyses of the relative permeabilities assigned to interfacing PTn model layers (cf. CRWMS M&O, 2000) and observed contact types led Fedors and Ferrill (2002) to conclude that the only modeled interface for which significant lateral flow might be expected is that between layers ptn21 and ptn22. A strong capillary barrier is plausible within the matrix continuum of the ptn21 massive ignimbrite, and the physical interface between the geologic units modeled by layers ptn21 and ptn22 is a sharp unconformity. Increased water content observed inconsistently in boreholes that pass through the base of the unit represented by the ptn21 model layer supports the *local* occurrence of this inferred capillary barrier (Fedors and Ferrill, 2002). All other interfaces that could have significant lateral flow based on relative permeabilities alone are actually associated with known gradational contacts (Fedors and Ferrill, 2002).

Two physically plausible locations for localized lateral flow caused by permeability or capillary barriers are (i) the tcw13/ptn21 model layer interface where fracture flow switches to predominantly matrix flow and (ii) the ptn26/tsw31 model interface where matrix flow switches to predominantly fracture flow. The active fracture model (cf., Liu et al., 1998) for fracture and matrix interaction, which is implemented in unsaturated zone flow models for Yucca Mountain, does not account for the physical processes that occur at these types of flow barriers (Fedors and Ferrill, 2002); thus, such flow models do not predict flow barriers at these plausible locations.

Deformation features, such as steeply dipping, small-displacement faults and fractures like those mapped and assessed at the Chalk Cove site (Dinwiddie et al., 2006) and at the Crucifix Site (herein and by McGinnis et al., in revision)—the effects of which are more easily modeled—cross all subunits of the PTn, as observed from surface exposures on the west flank of the volcanic ridge (Sweetkind et al., 1995), tunnel exposures within the Exploratory Studies Facility (Eatman et al., 1997; Barr et al., 1996), and vertical boreholes (cf., Engstrom and Rautman, 1996; Rautman and Engstrom, 1996a,b). From a detailed line survey in the Exploratory Studies Facility, Smart (2006) estimated 0.2, 0.3, and 0.3 faults per meter for partially reworked, bedded tuff unsaturated zone model layers ptn22, ptn24, and ptn26. For the PTn as whole, Fedors and Ferrill (2002) used this detailed line survey data to estimate an average fault dip of 70.2° for small-displacement faults. Fault strike in the PTn is perpendicular to bed dip, which should constrain lateral flow along bedding planes (Fedors and Ferrill, 2002). Smart (2006) corrected the raw full-periphery geologic mapped data from the Exploratory Studies Facility (Eatman et al., 1997; Barr et al., 1996) for orientation bias and determined the presence of three fracture sets in the PTn (i.e., two subvertical sets with average dips of approximately 80°, and one subhorizontal set with an average dip of approximately 10°). Steeply dipping or vertical fractures, whether open or filled, will promote vertical flow and constrain lateral flow (Fedors and Ferrill, 2002). Small-displacement faults and their related hydrologic properties and anisotropies, however, are also not typically represented in unsaturated zone flow models of Yucca Mountain. More realistic modeling of the PTn—its lithological properties, gradational contacts, and small-displacement, fault-related deformation structures—would significantly contribute to understanding the potential length scale for lateral flow in the PTn. We further advocate that the results of natural analog studies be consulted as an additional source of information concerning the unsaturated flow and transport properties of analog units in the Calico Hills Formation and Crater Flat Group located below the repository host horizon.

CONCLUSIONS

Analyses of tuffaceous sedimentary rock at the Crucifix Site reveal three classes of fault-zone deformation features, also observed in massive nonwelded ignimbrite units of the Bishop Tuff (Dinwiddie et al., 2006), that may constrain lateral flow in unsaturated bedded tuffs: (i) cataclasis resulting in fine-grained fault gouge, (ii) mappable open fractures, and (iii) microfractures, microfaults, and grain rotation resulting in additional connected porosity in matrix blocks adjacent the fault. Additional features of lithology-dependent fault zone deformation that further our qualitative understanding of expected flow behavior for bedded tuff units in the PTn were recognized in the tuffaceous sedimentary rock of the Crucifix Site, including

- Clay-smearing, bed dragging, and vertical segmentation of the Crucifix Fault plane
- Strongly asymmetrical damage associated with a horst-bounding fault, including the unusual observation of a footwall that exhibits major deformation and a hanging wall with negligible deformation [opposite to asymmetry observed by Dinwiddie et al. (2006)]
- Conjugate fractures clustered around numerous small-displacement conjugate faults in a 10-m-wide irregularly distributed footwall block, which should focus vertical

movement of water down dip and constrain lateral movement of water between faults that behave as flow barriers

- Pervasive vertical fractures throughout the entire exposure (> 100 m in width) that record a history of overburden, especially in areas where conjugate fracturing is minor, combine with conjugate fractures to increase fracture permeability
- Deformation-zone widths that vary as a function of bed lithology
- Small-scale deformation styles within matrix blocks that are likely influenced by bed thickness, grain size, levels of clay alteration, glass and ash content, and sintering intensity
- Deformation styles that may suggest brittle deformation behavior at the bed scale, but more ductile deformation behavior at the microscopic scale

Although it is likely that localized lateral flow along capillary or permeability barriers is associated with some subunits of the PTn, the presence of secondary heterogeneities in the form of small-displacement faults and fault-related deformation features throughout the unit, similar to those examined in these analog studies, suggests that lateral flow within the PTn at Yucca Mountain is unlikely over distances greater than the average small-displacement fault spacing in the downdip direction in each subunit. Consequently, the physical scale of lateral flow in the PTn may be smaller than the grid scale for mountain scale numerical models because small-displacement faults having spacings of tens of meters or less may induce vertical flow (Ofoegbu et al., 2001; Waiting et al., 2001; Fedors and Ferrill, 2002; Dinwiddie et al., 2006).

ACKNOWLEDGEMENTS

The authors gratefully acknowledge field assistance provided by Donald R. Bannon and Richard Heermance. Extensive discussions with Brittain E. Hill and James P. Evans are appreciated. This paper describes work performed by the Center for Nuclear Waste Regulatory Analyses (CNWRA) for the U.S. Nuclear Regulatory Commission (NRC) under Contract No. NRC–02–02–012. The activities reported here were performed on behalf of the NRC Office of Nuclear Material Safety and Safeguards, Division of High-Level Waste Repository Safety. This paper is an independent product of the CNWRA and does not necessarily reflect the view or regulatory position of the NRC. The NRC staff views expressed herein are preliminary and do not constitute a final judgment or determination of the matters addressed or of the acceptability of a license application for a geologic repository at Yucca Mountain.

REFERENCES

Antonellini, M.A. and A. Aydin, 1994. Effect of faulting on fluid flow in porous sandstones: Petrophysical properties. AAPG Bulletin 78(3):355–377.

Antonellini, M.A., A. Aydin, and D.D. Pollard, 1994. Microstructure of deformation bands in porous sandstones at Arches National Park, Utah. J. Structural Geology. 16(7):941–959.

Balsillie, J.H., J.F. Donoghue, K.M. Butler, and J.L. Koch, 2002. Plotting equation for Gaussian percentiles and a spreadsheet program for generating probability plots. J. Sedimentary Res. 72(6):929–933.

Barr, D.L., T.C. Moyer, W.L. Singleton, A.L. Albin, R.C. Lung, A.C. Lee, S.C. Beason, and G.L.W. Eatman, 1996. Geology of the North Ramp—Station 4+00 to 28+00, Exploratory Studies Facility, Yucca Mountain Project, Yucca Mountain, Nevada. DOE Report DTN GS960908314224.020. Denver, Colorado: Bureau of Reclamation and U.S. Geological Survey.

Beason, S.C., G.A. Turlington, R.C. Lung, G.L.W. Eatman, D. Ryter, and D.L. Barr, 1996. Geology of the North Ramp, Station 0+60 to 4+00, Exploratory Studies Facility, Yucca Mountain Project, Yucca Mountain, Nevada. Milestone Report 3GGF530M/3GGF540M. Denver, Colorado: U.S. Geological Survey. 13 Sept.

Bechtel SAIC Company, LLC, 2001. FY01 Supplemental Science and Performance Analysis. Vol. 1. Scientific Bases and Analyses. TDR-MGR-MD-000007. Rev. 0, ICN01. Las Vegas, Nevada.

Bechtel SAIC Company, LLC, 2003. Abstraction of Drift Seepage. MDL–NBS–HS–000019. Rev. 1. Las Vegas, Nevada.

Bechtel SAIC Company, LLC, 2004. Technical Basis Document No. 2: Unsaturated Zone Flow. Rev. 1. Las Vegas, Nevada.

Bense, V.F., 2005. Faults as conduit-barrier systems to fluid flow in siliciclastic sediments. Geological Society of America Abstracts with Programs 37(7):167, Abstract 67–6.

Boggs Jr., S., 1995. Principles of Sedimentology and Stratigraphy, Prentice-Hall Inc., Englewood Cliffs, NJ. 774 p.

Boggs Jr., S., 1992. Petrology of Sedimentary Rocks, Macmillan Publishing Co., New York, NY, 707 p.

Caine, J.S., J.P. Evans, and C.B. Forster, 1996. Fault zone architecture and permeability structure. Geology 24:1025–1028.

Caine, J.S., 2005. Implications for syn-faulting fluid flow from macroscopic fault rock textures and geochemistry: The San Ysidro fault, Albuquerque Basin, New Mexico. Geological Society of America Abstracts with Programs 37(7):167, Abstract 225–7.

Copeland, K., 2003. Fly Ash Properties and Uses. Internet Publication of the Monolithic Dome Institute. www.monolithic.com/construction/flyash/index.html (verified 28 June 2006). Monolithic Dome Institute, Italy, TX.

CRWMS M&O, 1998. Geology of the Exploratory Studies Facility Topopah Spring loop. BAB00000–01717–0100–00002. Rev 01. Las Vegas, Nevada. Civilian Radioactive Waste Management System Management and Operating Contractor.

CRWMS M&O, 2000. Unsaturated zone flow and transport model PMR. TDR-NBS-HS-000002. Rev 0. Las Vegas, Nevada. Civilian Radioactive Waste Management System Management and Operating Contractor.

Davatzes, N.C., A. Aydin, and P. Eichhubl, 2003. Overprinting faulting mechanisms during the development of multiple fault sets in sandstone, Chimney Rock fault array, Utah. Tectonophysics 363:1–18.

Davatzes, N.C., and A. Aydin, 2003. Overprinting faulting mechanisms in high porosity sandstones of SE Utah. J. Structural Geology 25:1795–1813.

Davis, S.N., 1969. Porosity and permeability in natural materials. *In* R.J.M. DeWiest (ed.) Flow through Porous Media, New York: Academic Press, 53–89.

Dawers, N.H., and M. Anders. 1995. Displacement-length scaling and fault linkage. J. Struct. Geol. 17:607–614.

Day, W.C., R.P. Dickerson, C.J. Potter, D.S. Sweetkind, C.A. San Juan, R.M. Drake, II, and C.J. Fridrich, 1998a. Bedrock geologic map of the Yucca Mountain area, Nye County, Nevada. U.S. Geological Survey Miscellaneous Investigations Series Map I-2627, scale 1:24,000.

Day, W.C., C.J. Potter, D.S. Sweetkind, R.P. Dickerson, and C.A. San Juan, 1998b. Bedrock geologic map of the Central Block Area, Yucca Mountain, Nye County, Nevada. U.S. Geological Survey Miscellaneous Investigations Series Map I–2601, scale 1:6000.

Dinwiddie, C.L., K.K. Bradbury, R.N. McGinnis, R.W. Fedors, and D.A. Ferrill, 2006. Fault zone deformation overprints permeability of nonwelded ignimbrite: Chalk Cove Fault, Bishop Tuff, Bishop, California. Available at www.vadosezonejournal.org. Vadose Zone J. 5:610–627.

Dinwiddie, C.L., 2005. The small-drillhole minipermeameter probe for in-situ permeability measurement. SPE Reservoir Evaluation & Engineering. 8(6):491–501.

Dinwiddie, C.L., F.J. Molz, III, and J.W. Castle, 2003. A new small drill hole minipermeameter probe for in situ permeability measurement: Fluid mechanics and geometrical factors. Water Resour. Res. 39(7), 1178, doi:10.1029/2001WR001179.

Du Bernard, X., P. Eichhubl, and A. Aydin, 2002. Dilation bands: A new form of localized failure in granular material. Geophys. Res. Lett. 29(24):1–4.

Eatman, G.L.W., W.L. Singleton, T.C. Moyer, D.L. Barr, A.L. Albin, R.C. Lung, and S.C Beason, 1997. Geology of the South Ramp–Station 55+00 to 78+77, Exploratory Studies Facility, Yucca Mountain Project, Yucca Mountain, Nevada. Denver, Colorado: Bureau of Reclamation and U.S. Geological Survey.

Engelder, T., 1974. Cataclasis and the generation of fault gouge. GSA Bulletin, 85:1515–1522.

Engstrom, D.A., and C.A. Rautman, 1996. Geology of the USW SD-9 Drill Hole, Yucca Mountain, Nevada. Sandia Report SAND96-2030, Prepared by Sandia National Laboratory, Albuquerque, New Mexico, for the U.S. Department of Energy, 128 p.

Evans, J.P., and K.K. Bradbury, 2004. Faulting and fracturing of nonwelded Bishop Tuff, Eastern California: Deformation mechanisms in very porous materials in the vadose zone. Available at www.vadosezonejournal.org. Vadose Zone J. 3:602–623.

Fedors, R.W., J. Evans, D. Or, C. Forster, J. Heath, and K.K. Bradbury, 2001. Unsaturated flow through fractured and unfractured non-welded tuffs. EOS Transactions of the American Geophysical Union, 2001 Fall Meeting Supplement, Abstract H52A–0365.

Fedors, R.W., and D.A. Ferrill, 2002. Potential for lateral flow associated with fractured, nonwelded, layered tuffs in the unsaturated zone. EOS Transactions of the American Geophysical Union, 2002 Fall Meeting Supplement, Abstract H52B.

Fedors, R.W., J.R. Winterle, W.A. Illman, C.L. Dinwiddie, and D.L. Hughson. 2002. Unsaturated zone flow at Yucca Mountain, Nevada: Effects of fracture heterogeneity and flow in the nonwelded Paintbrush tuff unit. CNWRA Letter Rep. US NRC Contract NRC-02-97-009, San Antonio, TX. Available at http://lsnnet.gov/ using LSN Accession Number NRC000007248 (verified 15 March 2006).

Ferrill, D.A., and A.P. Morris, 2001. Displacement gradient and deformation in normal fault systems. J. Structural Geology 23:619–638.

Ferrill, D.A., A. Morris, J.A. Stamatakos, and D. Sims, 2000. Crossing conjugate normal faults. AAPG Bulletin 84(10):1543–1559.

Ferrill, D.A., J.A. Stamatakos, and D. Sims, 1999a. Normal fault corrugation: Implications for growth and seismicity of active normal faults. J. Structural Geology 21:1027–1038.

Ferrill, D.A., J. Winterle, G. Wittmeyer, D. Sims, S. Colton, and A. Armstrong, 1999b. Stressed rock strains groundwater at Yucca Mountain, Nevada. GSA Today 9(5):2–7.

Fetter, C.W., 1994. Applied Hydrogeology. Macmillan College Publishing Company, New York, 691 pages.

Fisher, R., 1961. Proposed classification of volcaniclastic sediments and rocks. GSA Bull 72:1409–1414.

Fisher, R., 1966. Rocks composed of volcanic fragments and their classification. Earth Science Reviews 1:287–298.

Flint, L.E., A.L. Flint, J.S. Selker, 2003. Influence of transitional volcanic strata on lateral diversion at Yucca Mountain, Nevada. Water Resour. Res. 39(4), 1084, doi:10.1029/2002WR001503.

Flodin, E., and A. Aydin, 2004. Faults with asymmetric damage zones in sandstone, Valley of Fire State Park, southern Nevada. J. Structural Geology 26:983–988.

Gilbert, C.M., 1938. Welded tuff in eastern California. Geological Society of America Bulletin 49:1828–1862.

Gray, MB., J.A. Stamatakos, D.A. Ferrill, and M.A. Evans, 2005. Fault-zone deformation in welded tuffs at Yucca Mountain, Nevada, USA. J. Structural Geology 25:1873–1891.

Heynekamp, M.R., L.B. Goodwin, P.S. Mozley, and W.C. Haneburg, 1999. Controls on fault-zone architectures in poorly lithified sediments, Rio Grande Rift, New Mexico: Implications for fault-zone permeability and fluid flow. *In* W.C. Haneberg et al. (eds.) Faults and Subsurface Fluid Flow in the Shallow Crust, American Geophysical Union, Geophysical Monograph 113:27–49.

Hildreth, W., and G.A. Mahood, 1986. Ring-fracture eruption of the Bishop Tuff. Geological Society of America Bulletin 97:396–403.

Hinds, J.J., G.S. Bodvarsson, and G.H. Nieder-Westermann, 2003. Conceptual evaluation of the potential role of fractures in unsaturated processes at Yucca Mountain. J. Contam. Hydrol. 62/63:111–132.

Izett, G.A, J.D. Obradovich, and H.H. Mehnert, 1988. The Bishop ash bed and some older chemically and mineralogically similar ash beds in California, Nevada, and Utah. U.S. Geological Survey Bulletin 1675:37.

Lueddecke, S.B., N. Pinter, and P. Gans, 1998. Plio-Pleistocene ash falls, sedimentation, and range-front faulting along the White-Inyo Mountains front, California. J. Geology 106:511–522.

Levy, S., S. Chipera, G. WoldeGabriel, J. Fabryka-Martin, J. Roach, and D. Sweetkind, 1999. Flow-path textures and mineralogy in tuffs of the unsaturated zone. *In* W.C. Haneberg et al. (eds.) Faults and Subsurface Fluid Flow in the Shallow Crust, American Geophysical Union, Geophysical Monograph 113:159–184.

Liu, H.H., C. Doughty, and G.S. Bodvarsson, 1998. An active fracture model for unsaturated flow and transport in fractured rocks. Water Resour. Res. 34(10):2633–2646.

Main, I.G., K. Mair, O. Kwon, S.C. Elphick, and B.T. Ngwenya, 2001. Experimental constraints on the mechanical and hydraulic properties of deformation bands, in porous sandstones: A review. *In* R.E. Holdsworth et al. (eds.) The Nature and Significance of Fault Zone Weakening, Geol. Soc. Lond., Spec. Publ. 186:43–63.

Martel, S.J. 1989. Structure and late Quaternary activity of the northern Owens Valley fault zone, Owens Valley, California. Eng. Geol. 27:489–507.

McGinnis, Jr., R.N., D.A. Ferrill, A.P. Morris, and C.L. Dinwiddie, 2005. Deformation analysis of tuffaceous sediments in the Volcanic Tableland near Bishop, California. Geological Society of America Abstracts with Programs 37(7):210, Abstract 89–9.

McGinnis, R.N., D.A. Ferrill, A.P. Morris, and C.L. Dinwiddie, 2006. Deformation analysis of tuffaceous sediments in the Volcanic Tableland near Bishop, California. CNWRA IM 20.06002.01.262.520. In revision following peer review at J. Structural Geology.

Metz, J., and G.A. Mahood, 1985. Precursors to the Bishop Tuff eruption: Glass Mountain, Long Valley, California. J. Geophys. Res. 90:111,121–111,126.

Molz, F.J., L.C. Murdoch, C.L. Dinwiddie, and J.W. Castle, 2002. Small drill-hole, gas, mini-permeameter probe. US Statutory Invention Registration No. US H2052 H. Date issued: 3 Dec.

Morris, A.P., D.A. Ferrill, D.W. Sims, N. Franklin, and D.J. Waiting, 2004. Patterns of fault displacement and strain at Yucca Mountain, Nevada. J. Structural Geology 26:1707–1725.

Moyer, T.C., and J.K. Geslin, 1995. Lithostratigraphy of the Calico Hills Formation and Prow Pass Tuff (Crater Flat Group) at Yucca Mountain, Nevada: U.S. Geological Survey Open File Report 94-460, 59 p.

Moyer, T.C., J.K. Geslin, and L.O. Flint, 1996. Stratigraphic relations and hydrologic properties of the Paintbrush Tuff Nonwelded (PTn) hydrologic unit, Yucca Mountain, Nevada. United States Geological Survey Open-File Report 95-397, 151 p.

Muhunthan, B., R. Taha, and J. Said, 2004. Geotechnical engineering properties of incinerator ash mixes. J. Air and Waste Management Association 54(8):985–991.

Odling, N.E., S.D. Harris, and R.J. Knipe, 2004. Permeability scaling properties of fault damage zones in siliciclastic rocks. J. Structural Geology 26:1727–1747.

Ofoegbu, G.I., S. Painter, R. Chen, R.W. Fedors, and D.A. Ferrill, 2001. Geomechanical and thermal effects on moisture flow at the proposed Yucca Mountain nuclear waste repository. Nuclear Tech. 134(3):241–262.

Pinter, N. 1995. Faulting on the Volcanic Tableland, Owens Valley, California. J. Geol. 103:73–83.

Rautman, C.A., and D.A. Engstrom, 1996a. Geology of the USW SD-7 Drill Hole, Yucca Mountain, Nevada. Sandia Report SAND96-1474, Prepared by Sandia National Laboratory, Albuquerque, New Mexico, for the U.S. Department of Energy, 164 p.

Rautman, C.A., and D.A. Engstrom, 1996b. Geology of the USW SD-12 Drill Hole, Yucca Mountain, Nevada. Sandia Report SAND96-1368, Prepared by Sandia National Laboratory, Albuquerque, New Mexico, for the U.S. Department of Energy, 132 p.

Rawling, G., and L. Goodwin, 2003. Cataclasis and particulate flow in faulted, poorly lithified sediments. J. Structural Geology 25:317–331.

Sarna-Wojcicki, A., M.S. Pringle, J. Wijbrans, 2000. New ^{39}Ar/^{40}Ar age of the Bishop Tuff from multiple sites and sediment rate calibration for the Matuyama-Bruhnes boundary. J. Geophys. Res. 105(B9):21,431–21,444.

Schleicher, A.M., B.A. van der Pluijm, J.G. Solum, and L.N. Warr, 2006. The origin and significance of clay minerals on surfaces, in fractures and in veins from SAFOD borehole samples (Parkfield, California). Geophys. Res. Lett., in press.

Schmid, R., 1981. Descriptive nomenclature and classification of pyroclastic deposits and fragments: Recommendations of the IUGS Subcommission on the Systematics of Igneous Rocks. Geology 9(1):41–43.

Smart, K., 2006. PTn-Related Structural and Hydrogeological Characterization: Structural Geology of the PTn. *In* C. Manepally, K. Bradbury, S. Colton, C. Dinwiddie, R. Green, R. McGinnis, D. Sims, K. Smart and G. Walter, The Nature of Flow in the Faulted and Fractured Paintbrush Nonwelded Hydrogeologic Unit. CNWRA Letter Rep. US NRC Contract NRC–02–02–012, San Antonio, TX. Available at http://lsnnet.gov/ using LSN Accession Number NRC00000xxxx (verified xx Month 200x).

Smith, G.A., 1986. Coarse-grained nonmarine volcaniclastic sediment: Terminology and depositional process. Geological Society of America Bulletin 97:1–10.

Spengler, R.W., C.A. Braun, R.M. Linden, L.G. Martin, D.M. Ross-Brown, and R.L. Blackburn, 1993. Structural characterization of the Ghost Dance Fault, Yucca Mountain, Nevada. *In* Proc Fourth International High-Level Radioactive Waste Management Conference, Las Vegas, NV. 26–30 Apr., p. 653–659.

Sweetkind, D.S., E.R. Verbeek, J.K. Geslin, and T.C. Moyer, 1995. Fracture character of the Paintbrush Tuff nonwelded hydrogeologic unit, Yucca Mountain, Nevada. U.S. Geological Survey Administrative Report to the U.S. Department of Energy, 202pp.

Vaniman, D.T., S.J. Chipera, D.L. Bish, J.W. Carey, and S.S. Levy, 2001. Quantification of unsaturated-zone alteration and cation exchange in zeolitized tuffs at Yucca Mountain, Nevada, USA, Geochemica et Cosmochemica Acta 65(20):3409–3433.

Waiting, D.J., R. Chen, J.G. Crider, W.M. Dunne, R.W. Fedors, D.A. Ferrill, M.B. Gray, B.E. Hill, P.C. LaFemina, H.L. McKague, A.P. Morris, D.W. Sims, and J.A. Stamatakos, 2001. Technical assessment of structural deformation and seismicity at Yucca Mountain, Nevada. CNWRA Letter Rep. US NRC Contract NRC-02-97-009, San Antonio, TX. Available at http://lsnnet.gov/ using LSN Accession Number NRC000017443 (verified 27 Mar. 2006).

Wilson, C.J.N, and W. Hildreth, 1997. The Bishop Tuff: New insights from eruptive stratigraphy. J. Geology 105:407–439.

Wilson, C.J.N, and W. Hildreth, 1998. Hybrid fall deposits in the Bishop Tuff, California: A novel pyroclastic depositional mechanism. Geology 26(1):7–10.

Wilson, C.J.N, and W. Hildreth, 2003. Assembling an ignimbrite: Mechanical and thermal building blocks in the Bishop Tuff, California. J. Geology 111:653–670.

Wilson, J.E, L.B. Goodwin, and C.J. Lewis, 2003. Deformation bands in nonwelded ignimbrites: Petrophysical controls on fault-zone deformation and evidence of preferential fluid flow. Geology 31(10):837–840. Mountain, Nevada. LBNL-46876. Berkeley, California, Lawrence Berkeley National Laboratory.

Wolf, H., 2003. Experimental investigation of shear band patterns in granular material. J. Structural Geology 25(8):1229–1240.

Wu, Y.-S., W. Zhang, L. Pan, J. Hinds, and G.S. Bodvarsson, 2002. Modeling capillary barriers in unsaturated fractured rock, Water Resour. Res. 38(11):1253–1263.

Yanagimoto, A., and A. Iijima, 2003. Hydrothermal laumontization and microfracture formation in reservoir rocks at the Yufutsu Field, Hokkaido, northern Japan. J. Petroleum Geology 26(3):351.

Yielding, G., B. Freeman, and D.T. Needham, 1997. Quantitative fault seal prediction. AAPG Bulletin 81(6):897–917.

FIGURE CAPTIONS

Fig. 1. (a) Stratigraphy of the Paintbrush nonwelded hydrogeologic unit (after Dinwiddie, et al. 2006) with emphasis on the bedded tuffs. (b) Block diagram depicting the Glass Mountain Rhyolite-derived reworked tuffaceous sedimentary rock and horst-bounding faults of the Crucifix Site in relation to the overlying Bishop Tuff (after McGinnis et al., in revision).

Fig. 2. Aerial photograph looking north across the southern boundary of the Volcanic Tableland and illustrating the Crucifix Site study area (after McGinnis et al., in revision). Inset coordinates are UTM Zone 11 NAD 83.

Fig. 3. (a) Cut bank at Crucifix Site. USGS 7½-minute Fish Slough quadrangle topographic map (1:24,000) has a 10-m contour interval with a 2-m supplementary interval. (b) Plan view map of the Crucifix Site. The 110-m-long outcrop exposure is represented by a gray line. The two bounding faults are represented by blue lines; the ball and bar are on the downthrown side of each fault. Fault clusters are represented by green boxes; we focused on the Crucifix Fault and two coherent beds east of this fault to a distance of 16.5 m (sketch after McGinnis et al., in revision).

Fig. 4. Crucifix Fault and 10.5 m of footwall block. (a) Photomosaic (after McGinnis et al., in revision) with grain size and permeability sample locations identified. (b) Lithostratigraphic map emphasizing Beds CF1 and CF2 and lithologic sample locations.

Fig. 5. Crucifix Fault (see Figure 4b for context). (a) Sample collection locations for three thin sections and permeabilities measured in three drill holes are indicated. (b) The fault core includes multiple layers and its properties change vertically and horizontally. Beds of reworked volcaniclastics are entrained within the mixed outer zones of the Crucifix Fault core, whereas clay gouge composes the central zone. The millimeter-thick bounding slip surfaces of the fault are mineralized by calcite, suggesting fluid flow interactions along the fault [after Fig. 7 of Evans and Bradbury (2004)].

Fig. 6. Areal fracture density within 25-cm-diameter circles centered around permeability test holes, as calculated from the trace length and fracture set data of McGinnis et al. (in revision). Red points denote drill holes intersecting fault zones; all data shown were used to derive the arithmetic mean grain size for each bed.

Fig. 7. (a) Primary heterogeneity displayed in terms of average grain size for samples collected from the outcrop surface at each permeability test hole in Beds CF1 and CF2. Red points, however, represent the average grain size of fault material located in the associated beds—these data were not used to derive the geometric mean grain size for each bed. (b) Sorting information, given as the standard deviation of grain size measure ϕ for each sample, indicates that Bed CF1 is more poorly sorted than Bed CF2, and sorting is predictable as a function of grain size. (c) Weight percent fines of samples from Beds CF1 and CF2. Arithmetic mean is not based on fault samples. (d) Weight percent fines ($< 4\phi$) as a function of mean grain size.

Fig. 8. Compositions and textures of Beds CF1 and CF2. (a) Bed CF1 (Sample BT-93; see Figure 4b for location): Dark-colored material near a fracture surface likely results from iron-oxide or clay alteration. Blue epoxy infiltrates the matrix from the wall of a hairline fracture surface. (b) CF2 (Sample BT-62): Dark-brown coating around grains indicates alteration and formation of clay rims. Alteration of glass (alt) within a flattened pumice clast or fiamma (F) also suggests the initial stages of clay formation. Microfracturing (Fr), shown near the fiamma boundary, is commonly observed in this material. Microfracture is partially filled with dark-brown clay and iron oxides alternating with silica.

Fig. 9. Photomicrographs of fault located at ~9.65 m (Figure 4b). (a) Sample BT-91 collected from contact of 1-cm-thick fault surface with Bed CF2. Crystal fragments and glass shards are supported by a fine-grained matrix of glass and clay. A zone of fine-grained clay surrounds the outer walls of open hairline microfracture surfaces (Fr), illustrating a mixed zone of deformation, including cataclasis and dilation. The wormlike texture labeled K is vermicular kaolinite. The well-developed vermicular texture suggests the clay is authigenic pore-filling cement that formed in situ, likely a result of diagenesis. (b) Sample BT-90 exhibits an amorphous silicic glassy fragment (G) with overgrowth textures, shown by an arrow pointing to the original grain boundary. P = pumice clast; Fr = fracture and dilation band.

Fig. 10. Cataclastic deformation mechanisms and fracture fillings. Sample BT-106 was collected near the eastern conjugate fault at ~4.7 m (Figure 4b). A large curvilinear fracture illustrates entrainment of grains from wall boundaries and is filled with iron oxides, clay, and glass altering to zeolite. Blue epoxy fills oblique microfractures.

Fig. 11. Crucifix Fault core. (a) Sample BT-104a was collected from the eastern-most layer inside the Crucifix Fault core (Figure 4b). Abrasion, mixing, and dragging of adjacent beds, as observed at the outcrop scale, results in abundant crystal and glass fragments observed at the micrometer scale. (b) Anastomosing fracture patterns (Sample BT-104). Blue epoxy pattern illustrates partial fracture filling. (c) Sample BT-105 was collected perpendicular to fault strike on west edge of Crucifix Fault. A halo of light-colored, convoluted clay and glassy ash surround an intracore microfracture, which is then surrounded by another halo of micrometer-thick bleached material. The microfracture does not absorb the blue epoxy, unlike the surrounding clay layer.

Fig. 12. Crucifix Fault deformation microstructures illustrate layered heterogeneity with varying textural and lithological characteristics. (a) Sample BT-107a, from a western section of gouge (Figures 4b and 5a), shows perlitic fracturing in a glassy fragment. Open microfractures absorb blue epoxy, while filled fractures do not. A brownish matrix of clay, volcanic ash, and glass is observed, and crystal fragments are abundant. (b) Sample BT-107b, from the central fault core gouge zone (Figures 4b and 5a), illustrates a layered and locally convoluted, fine-grained clay and ash having multiple fractures filled with silica and bounded by layers of clay—shown in alternating light and dark colors. Iron-oxide-rich clays are shown in the upper microfracture and in an altered glassy fragment. Blue epoxy in the upper half of the photomicrograph does not extend below the fracture oblique to the sections. (c) Sample BT-107c, shown in cross-polarized light with the gypsum plate inserted. A deformed feldspar clast with sericitic alteration is surrounded by a zone of fine-grained cataclasis that is characterized by rotated grains and microfractures, pumice and glass fragments, quartz clast, and fine-grained clay.

Fig. 13. Permeability data measured in Beds CF1 and CF2 illustrate how this parameter varies in the footwall of the Crucifix Fault. Red points represent data from test holes intersecting fault material located in the associated beds—these data are hybrid combinations of permeability from fault material and permeability of adjacent nonfaulted bed material and were not used to derive the geometric mean permeability for each bed.

Fig. 14. Crossplots of permeability and areal fracture density illustrate the general absence of direct correlation between these measured properties. (a) Crossplot for Bed CF1 and conjugate fractures with data split into two bins on the basis of faulting intensity. (b) Crossplot for Bed CF1 and vertical fractures. (c) Crossplot for Bed CF2 and conjugate fractures. An intensely faulted zone between 0 and ~6 m along the transect shows a slight correlation with permeability and ~20% of the observed variation in this zone is explained by a linear regression. (d) Crossplot for Bed CF2 and vertical fractures.

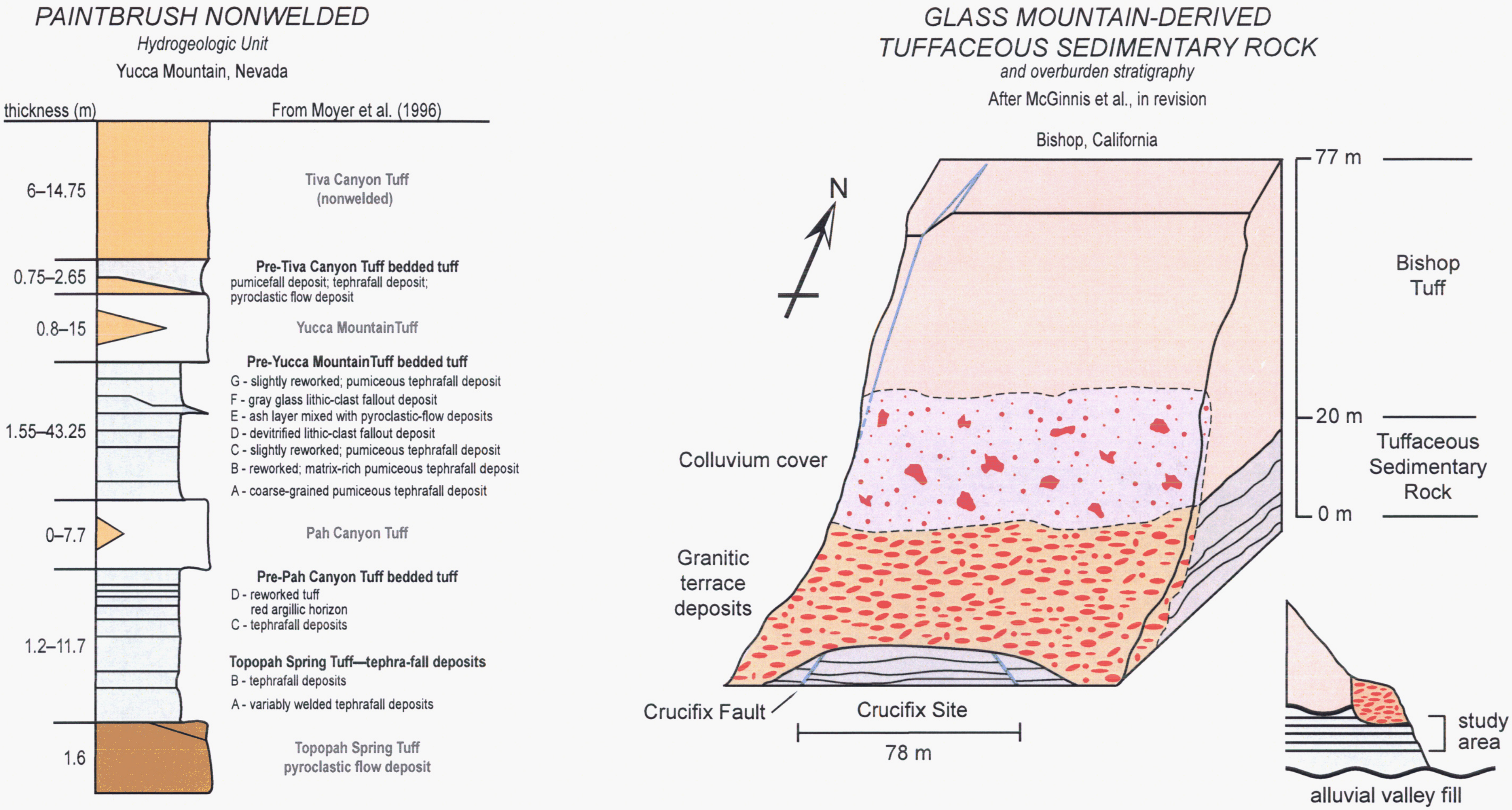

Fig. 1. (a) Stratigraphy of the Paintbrush nonwelded hydrogeologic unit (after Dinwiddie et al., 2006) with emphasis on the bedded tuffs. (b) Block diagram depicting the Glass Mountain Rhyolite-derived reworked tuffaceous sedimentary rock and horst-bounding faults of the Crucifix Site in relation to the overlying Bishop Tuff (after McGinnis et al., in revision).

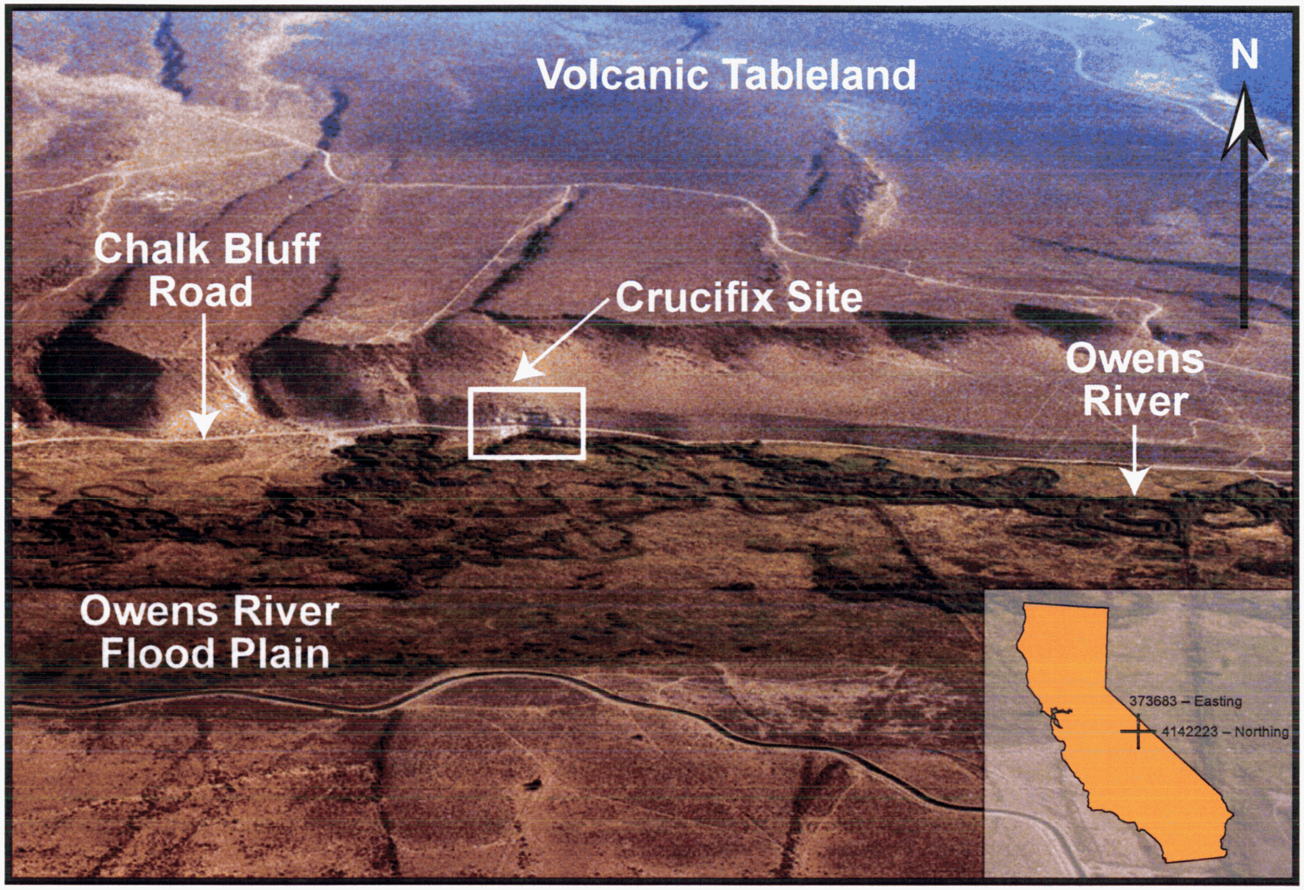

Fig. 2. Aerial photograph looking north across the southern boundary of the Volcanic Tableland and illustrating the Crucifix Site study area (after McGinnis et al., in revision). Inset coordinates are UTM Zone 11 NAD 83.

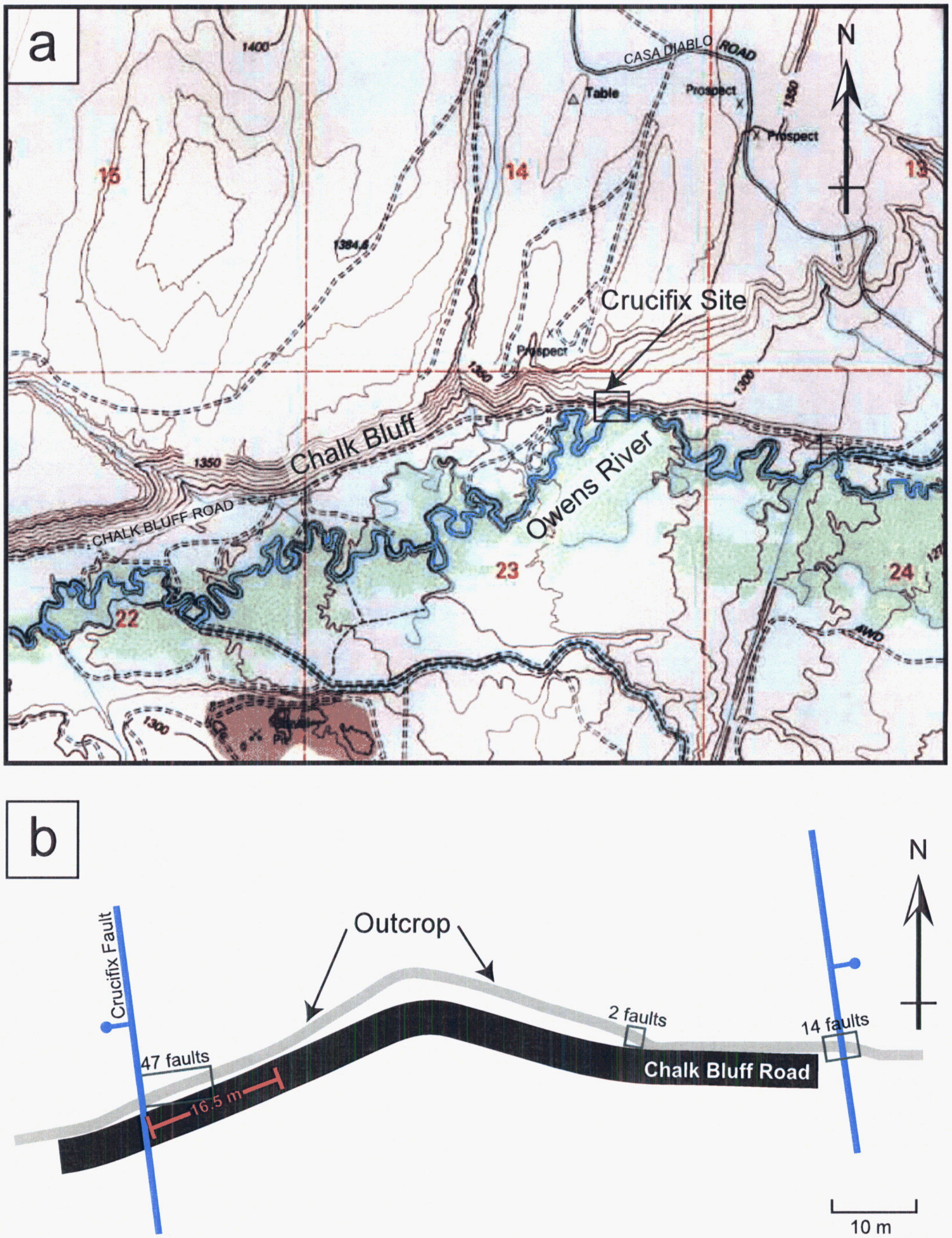

Fig. 3. (a) Cut bank at Crucifix Site. USGS 7½-minute Fish Slough quadrangle topographic map (1:24,000) has a 10-m contour interval with a 2-m supplementary interval. (b) Plan view map of the Crucifix Site. The 110-m-long outcrop exposure is represented by a gray line. The two bounding faults are represented by blue lines; the ball and bar are on the downthrown side of each fault. Fault clusters are represented by green boxes; we focused on the Crucifix Fault and two coherent beds east of this fault to a distance of 16.5 m (sketch after McGinnis et al., in revision).

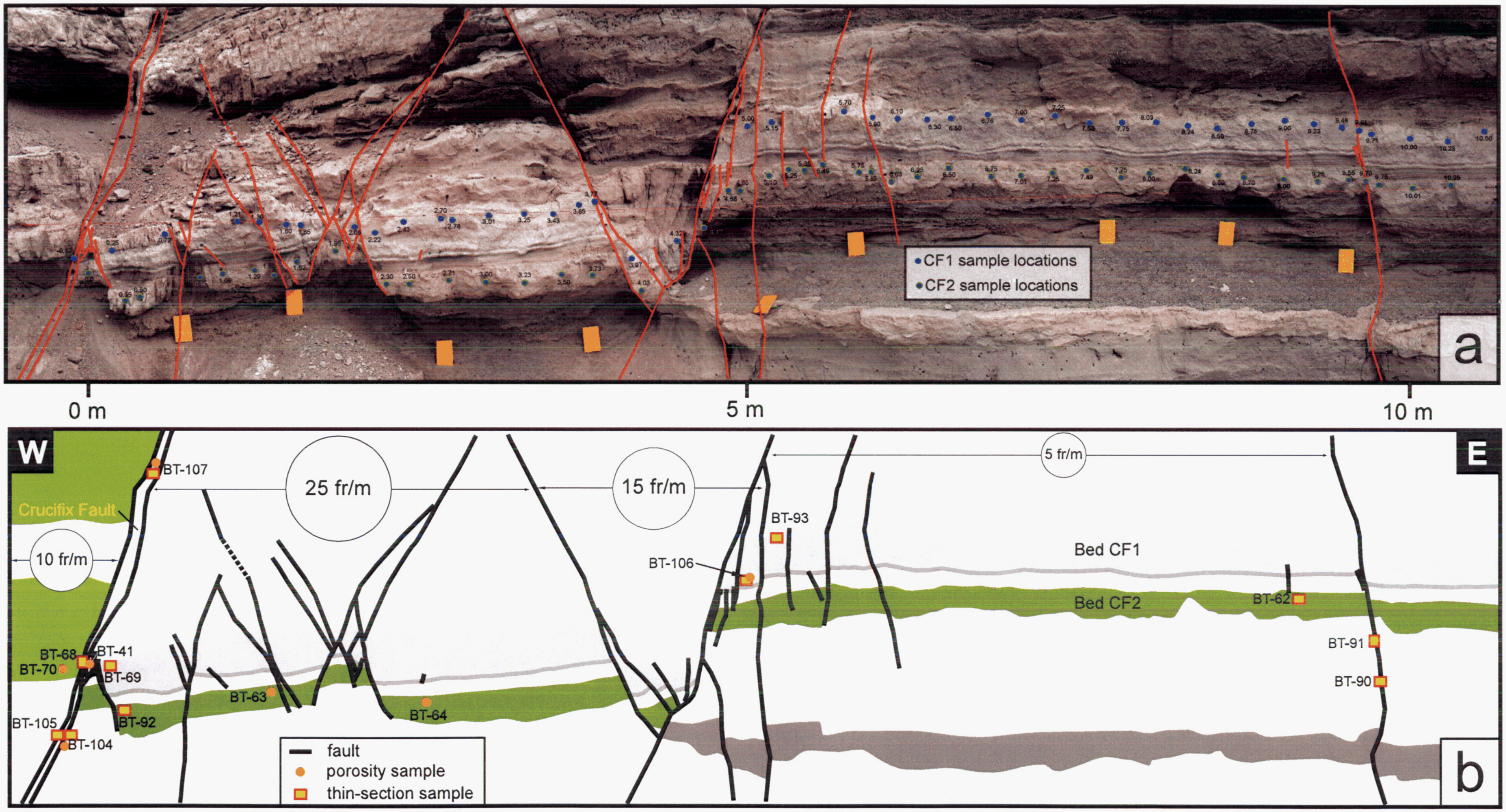

Fig. 4. Crucifix Fault and 10.5 m of footwall block. (a) Photomosaic (after McGinnis et al., in revision) with grain size and permeability sample locations identified. (b) Lithostratigraphic map emphasizing Beds CF1 and CF2 and lithologic sample locations.

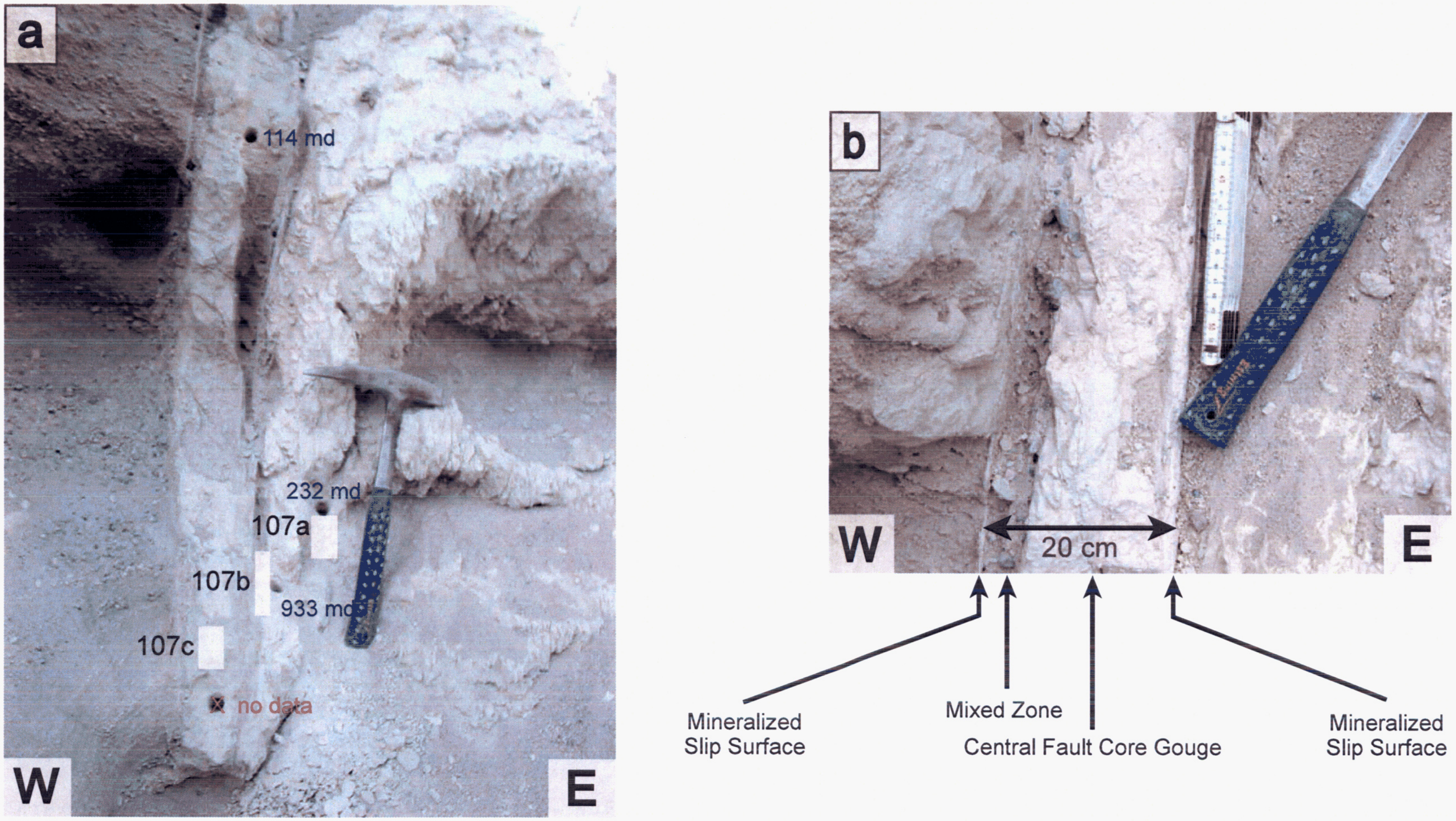

Fig. 5. Crucifix Fault (see Figure 4b for context). (a) Sample collection locations for three thin sections and permeabilities measured in three drill holes are indicated. (b) The fault core includes multiple layers and its properties change vertically and horizontally. Beds of reworked volcaniclastics are entrained within the mixed outer zones of the Crucifix Fault core, whereas clay gouge composes the central zone. The millimeter-thick bounding slip surfaces of the fault are mineralized by calcite, suggesting fluid flow interactions along the fault [after Fig. 7 of Evans and Bradbury (2004)].

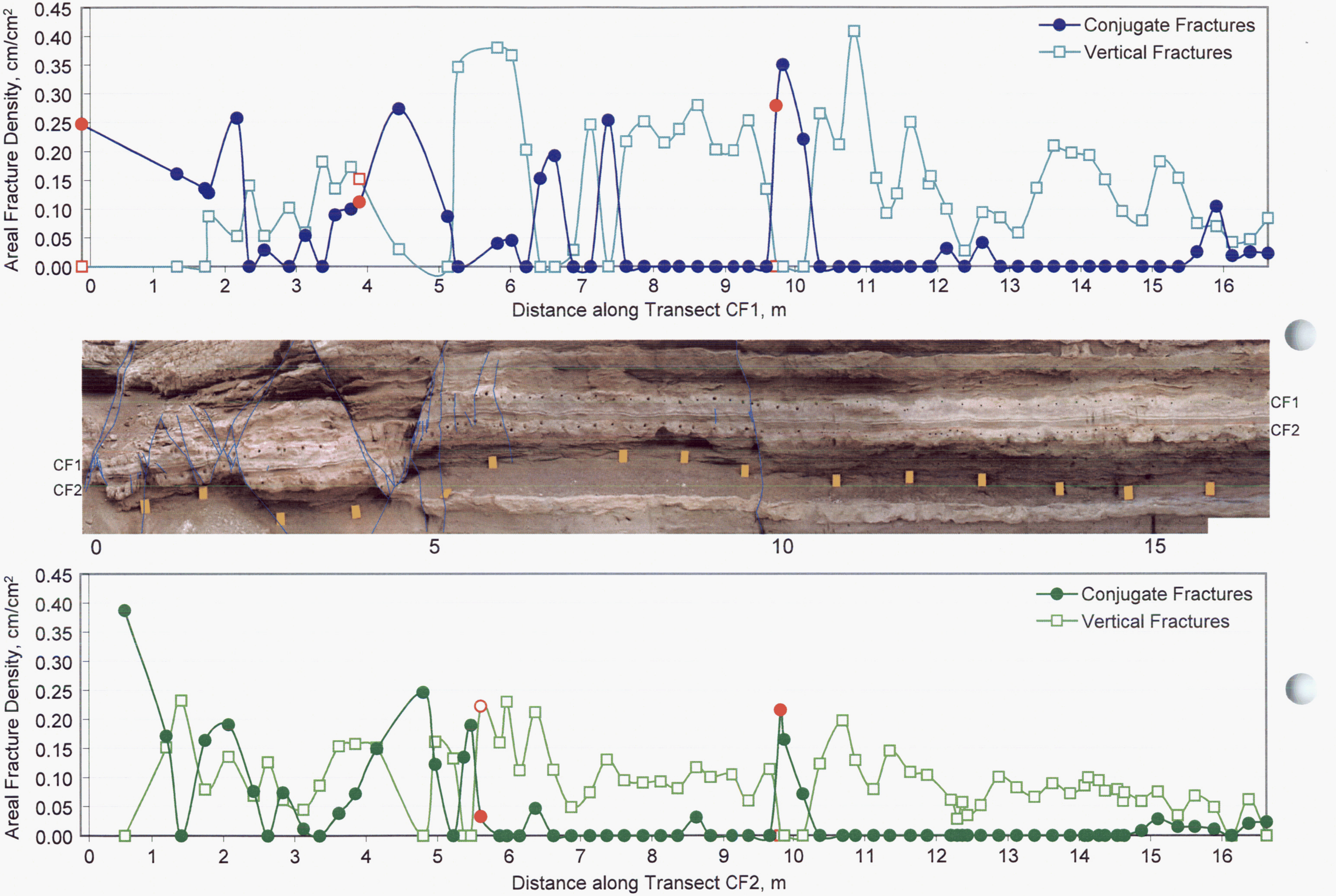

Fig. 6. Areal fracture density within 25-cm-diameter circles centered around permeability test holes, as calculated from the trace length and fracture set data of McGinnis et al. (in revision). Red points denote drill holes intersecting fault zones; all data shown were used to derive the arithmetic mean grain size for each bed.

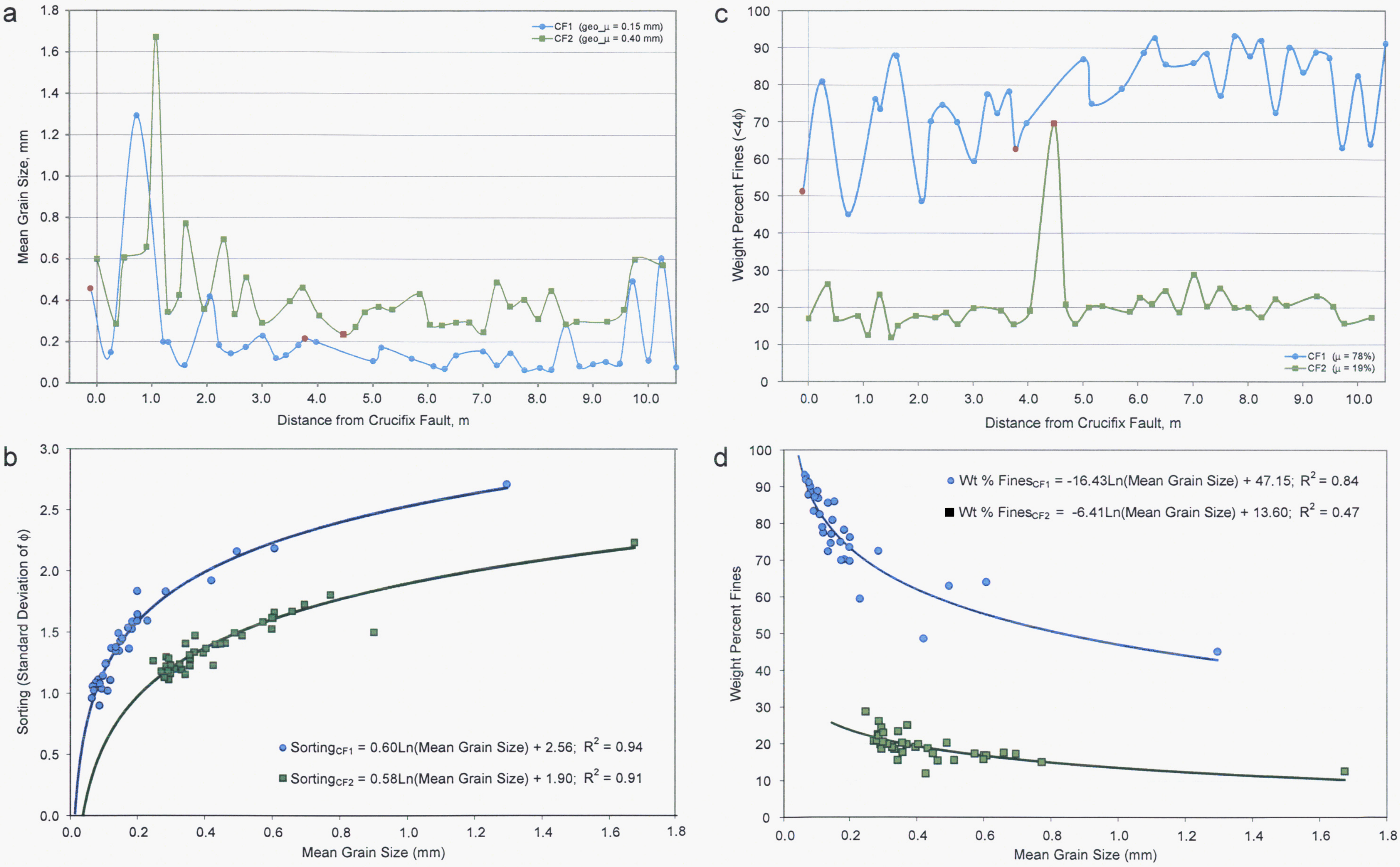

Fig. 7. (a) Primary heterogeneity displayed in terms of average grain size for samples collected from the outcrop surface at each permeability test hole in Beds CF1 and CF2. Red points, however, represent the average grain size of fault material located in the associated beds—these data were not used to derive the geometric mean grain size for each bed. (b) Sorting information, given as the standard deviation of grain size measure ϕ for each sample, indicates that Bed CF1 is more poorly sorted than Bed CF2, and sorting is predictable as a function of grain size. (c) Weight percent fines of samples from Beds CF1 and CF2. Arithmetic mean is not based on fault samples. (d) Weight percent fines (< 4ϕ) as a function of mean grain size.

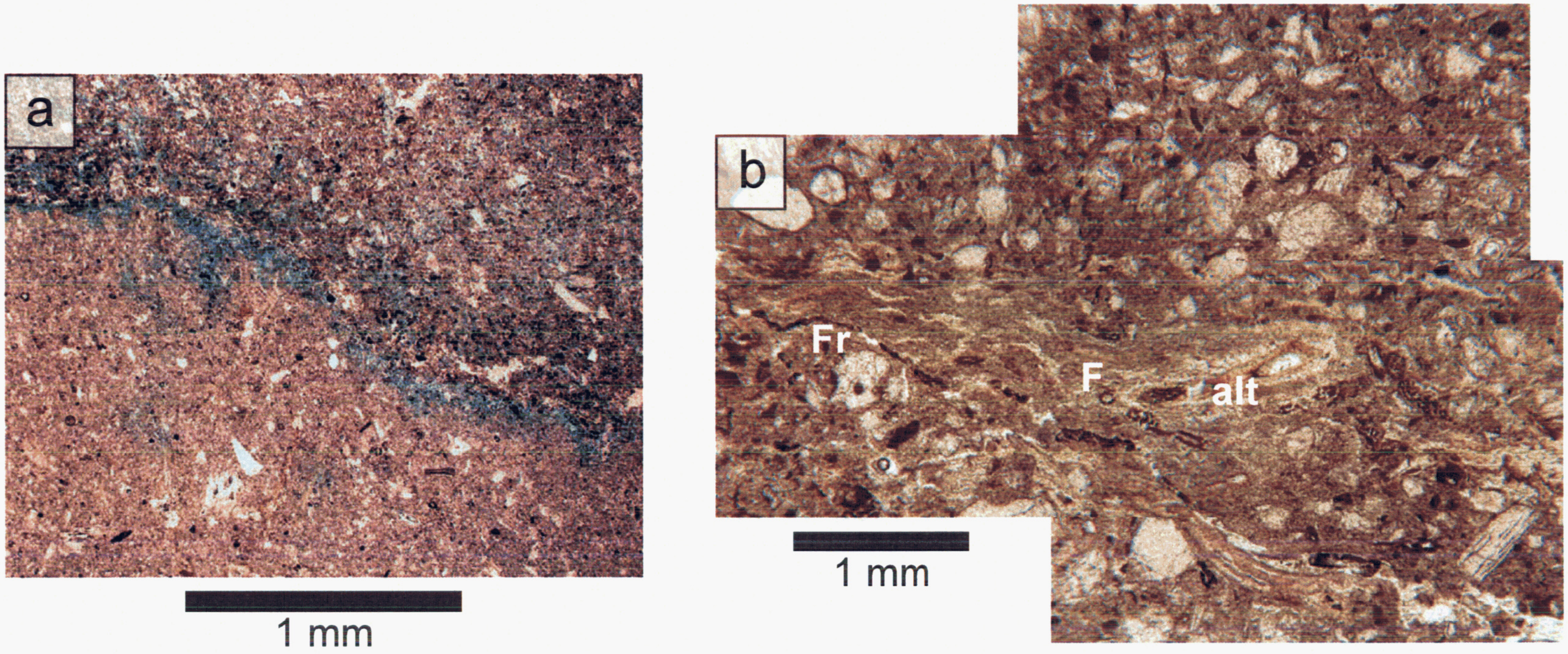

Fig. 8. Compositions and textures of Beds CF1 and CF2. (a) Bed CF1 (Sample BT-93; see Figure 4b for location): Dark-colored material near a fracture surface likely results from iron-oxide or clay alteration. Blue epoxy infiltrates the matrix from the wall of a hairline fracture surface. (b) CF2 (Sample BT-62): Dark-brown coating around grains indicates alteration and formation of clay rims. Alteration of glass (alt) within a flattened pumice clast or fiamma (F) also suggests the initial stages of clay formation. Microfracturing (Fr), shown near the fiamma boundary, is commonly observed in this material. Microfracture is partially filled with dark-brown clay and iron oxides alternating with silica.

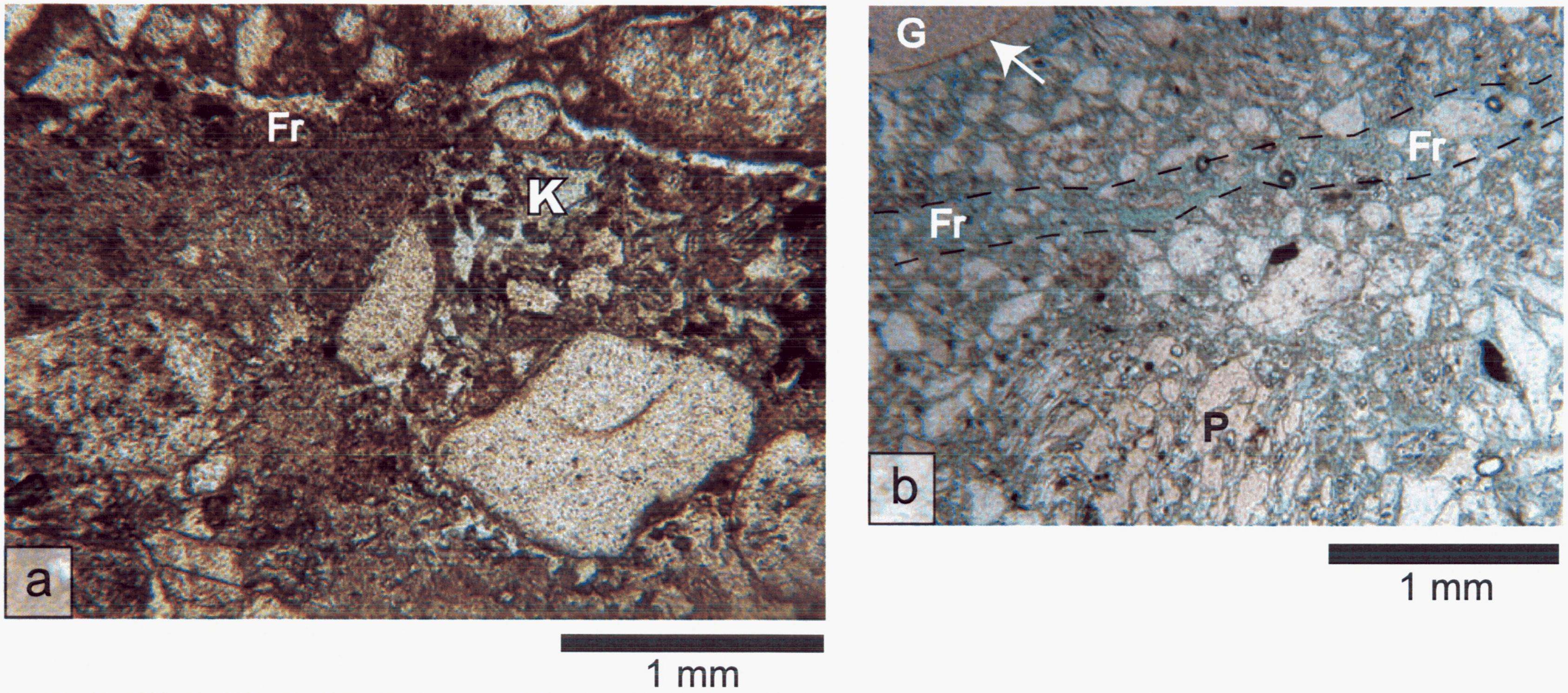

Fig. 9. Photomicrographs of fault located at ~9.65 m (Figure 4b). (a) Sample BT-91 collected from contact of 1-cm-thick fault surface with Bed CF2. Crystal fragments and glass shards are supported by a fine-grained matrix of glass and clay. A zone of fine-grained clay surrounds the outer walls of open hairline microfracture surfaces (Fr), illustrating a mixed zone of deformation, including cataclasis and dilation. The wormlike texture labeled K is vermicular kaolinite. The well-developed vermicular texture suggests the clay is authigenic pore-filling cement that formed in situ, likely a result of diagenesis. (b) Sample BT-90 exhibits an amorphous silicic glassy fragment (G) with overgrowth textures, shown by an arrow pointing to the original grain boundary. P = pumice clast; Fr = fracture and dilation band.

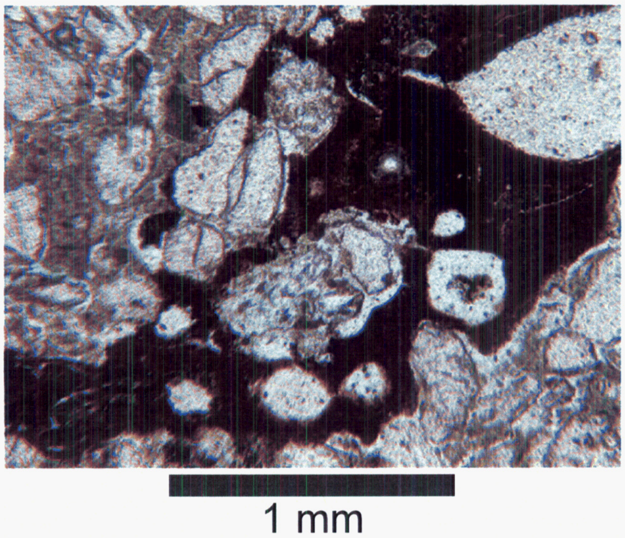

Fig. 10. Cataclastic deformation mechanisms and fracture fillings. Sample BT-106 was collected near the eastern conjugate fault at ~4.7 m (Figure 4b). A large curvilinear fracture illustrates entrainment of grains from wall boundaries and is filled with iron oxides, clay, and glass altering to zeolite. Blue epoxy fills oblique microfractures.

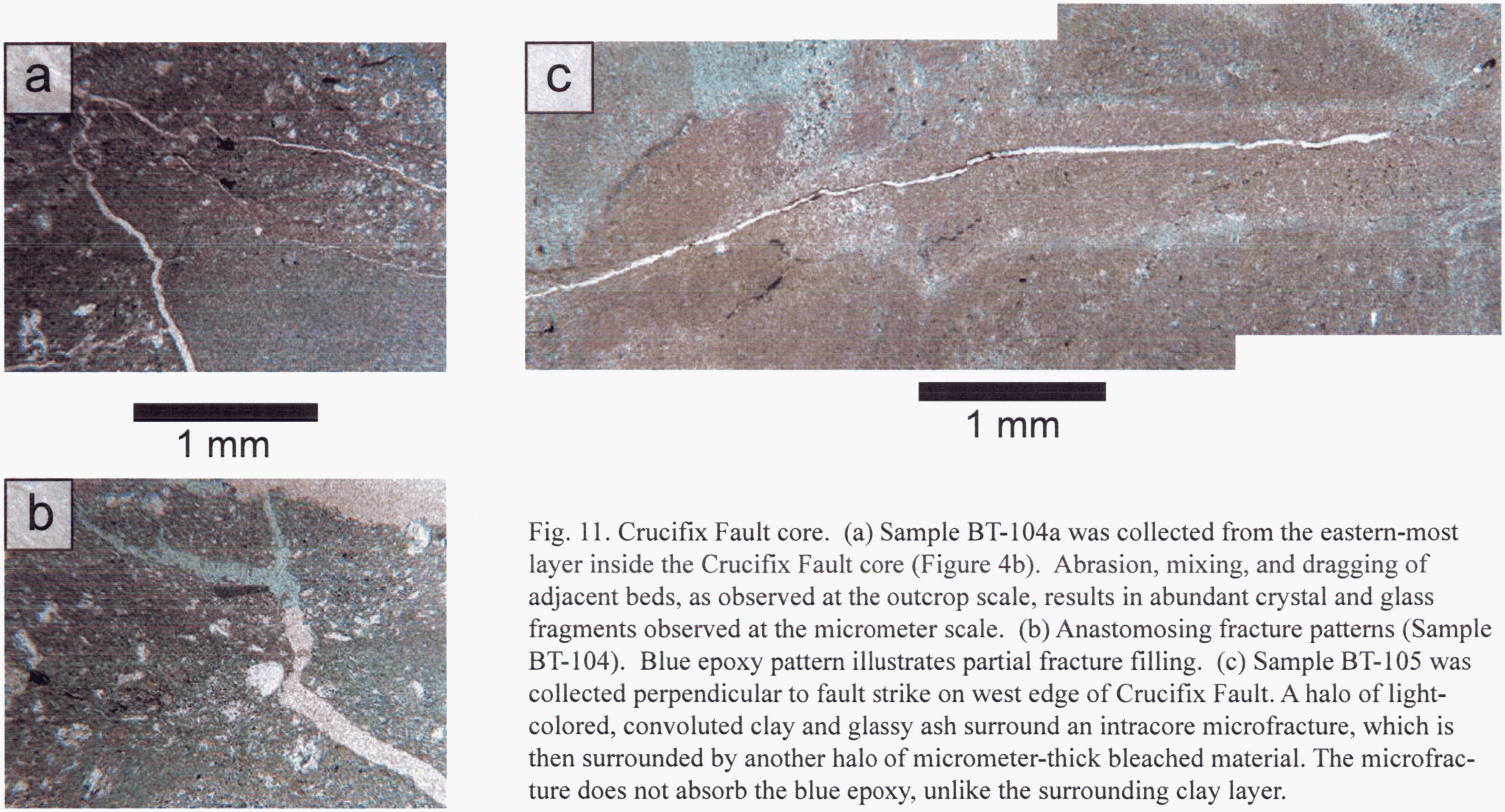

Fig. 11. Crucifix Fault core. (a) Sample BT-104a was collected from the eastern-most layer inside the Crucifix Fault core (Figure 4b). Abrasion, mixing, and dragging of adjacent beds, as observed at the outcrop scale, results in abundant crystal and glass fragments observed at the micrometer scale. (b) Anastomosing fracture patterns (Sample BT-104). Blue epoxy pattern illustrates partial fracture filling. (c) Sample BT-105 was collected perpendicular to fault strike on west edge of Crucifix Fault. A halo of light-colored, convoluted clay and glassy ash surround an intracore microfracture, which is then surrounded by another halo of micrometer-thick bleached material. The microfracture does not absorb the blue epoxy, unlike the surrounding clay layer.

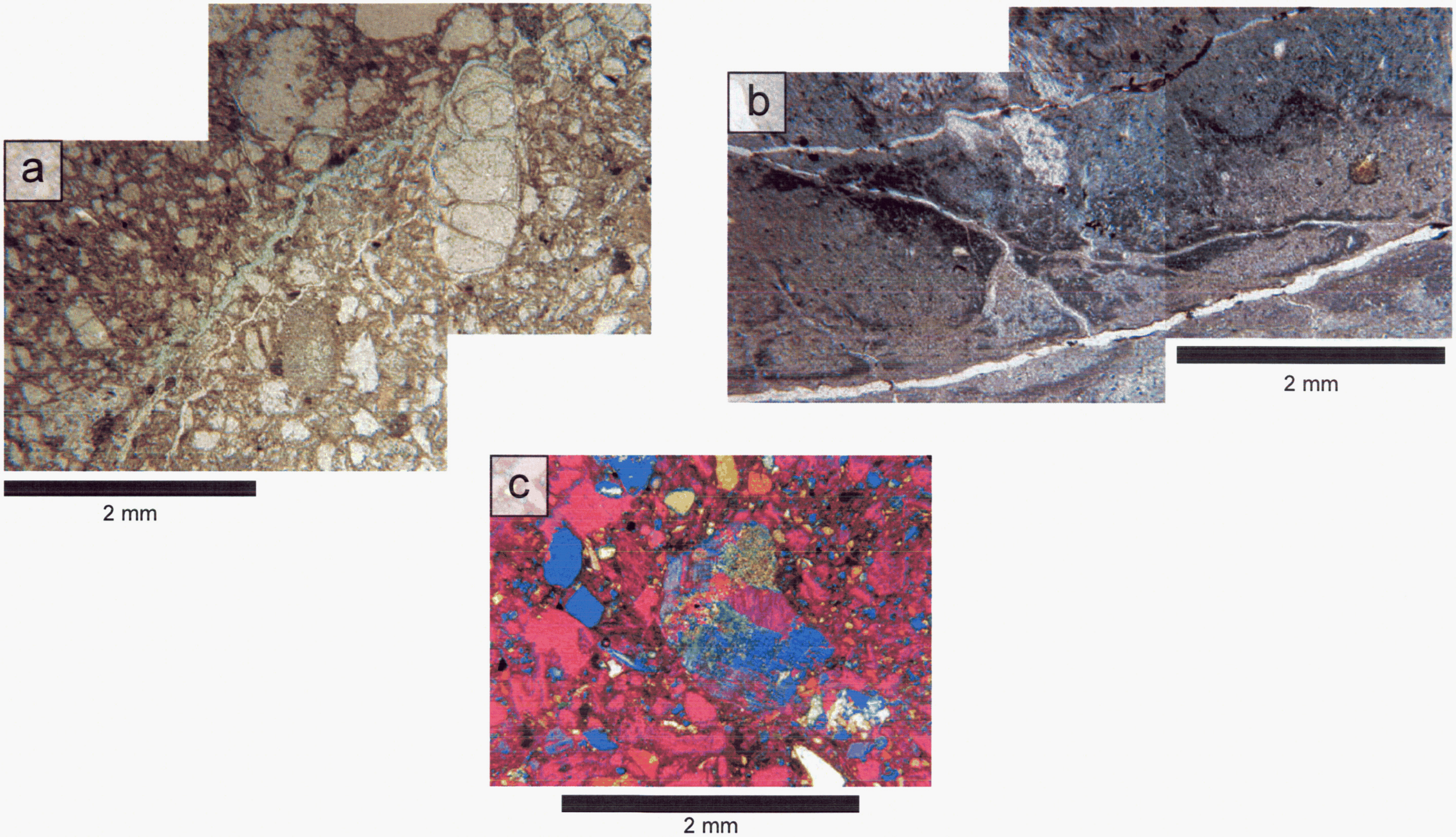

Fig. 12. Crucifix Fault deformation microstructures illustrate layered heterogeneity with varying textural and lithological characteristics. (a) Sample BT-107a, from a western section of gouge (Figures 4b and 5a), shows perlitic fracturing in a glassy fragment. Open microfractures absorb blue epoxy, while filled fractures do not. A brownish matrix of clay, volcanic ash, and glass is observed, and crystal fragments are abundant. (b) Sample BT-107b, from the central fault core gouge zone (Figures 4b and 5a), illustrates a layered and locally convoluted, fine-grained clay and ash having multiple fractures filled with silica and bounded by layers of clay—shown in alternating light and dark colors. Iron-oxide-rich clays are shown in the upper microfracture and in an altered glassy fragment. Blue epoxy in the upper half of the micrograph does not extend below the fracture oblique to the sections. (c) Sample BT-107c, shown in cross-polarized light with the gypsum plate inserted. A deformed feldspar clast with sericitic alteration is surrounded by a zone of fine-grained cataclasis that is characterized by rotated grains and microfractures, pumice and glass fragments, quartz clast, and fine-grained clay.

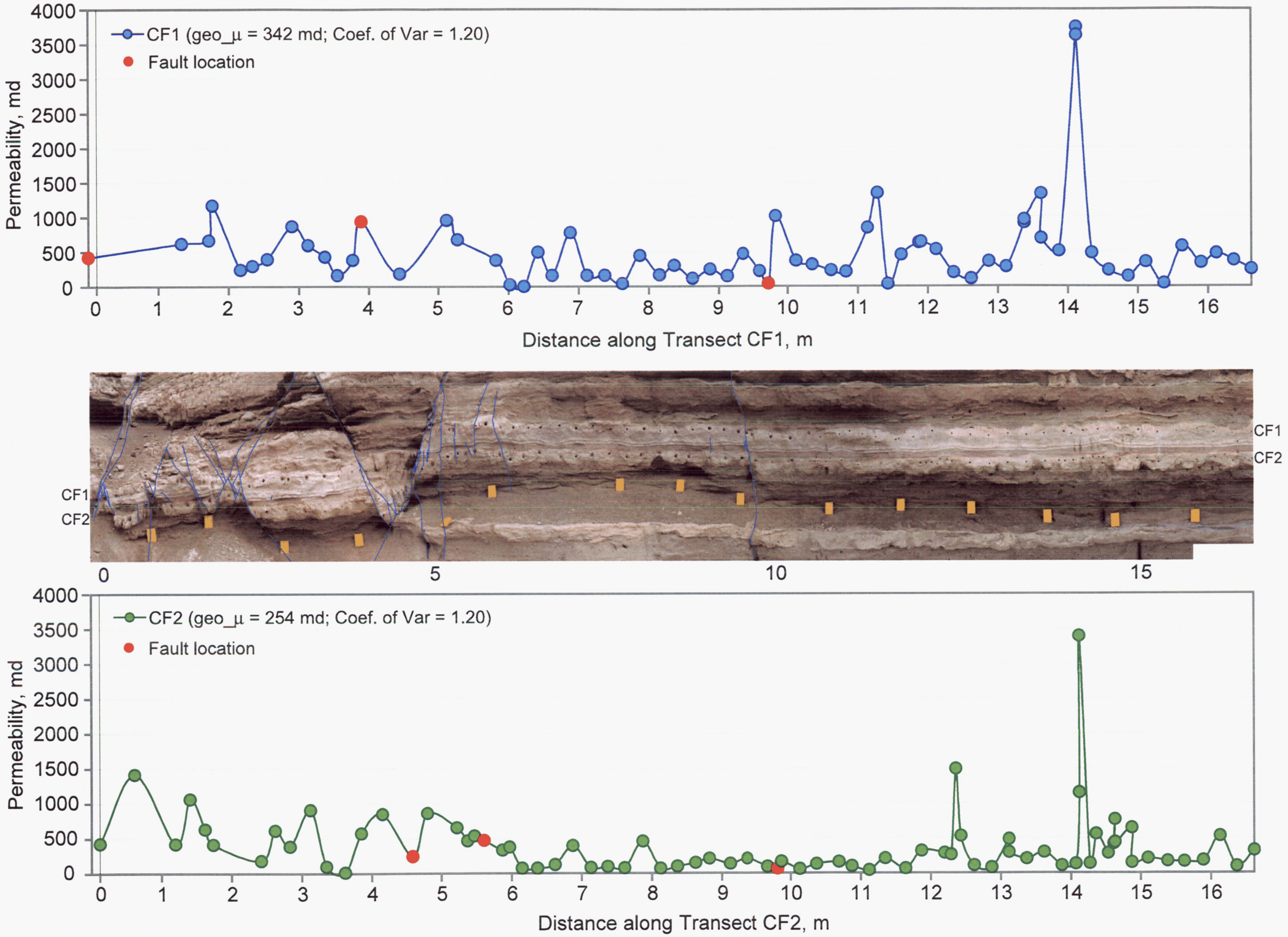

Fig. 13. Permeability data measured in Beds CF1 and CF2 illustrate how this parameter varies in the footwall of the Crucifix Fault. Red points represent data from test holes intersecting fault material located in the associated beds—these data are hybrid combinations of permeability from fault material and permeability of adjacent nonfaulted bed material and were not used to derive the geometric mean permeability for each bed.

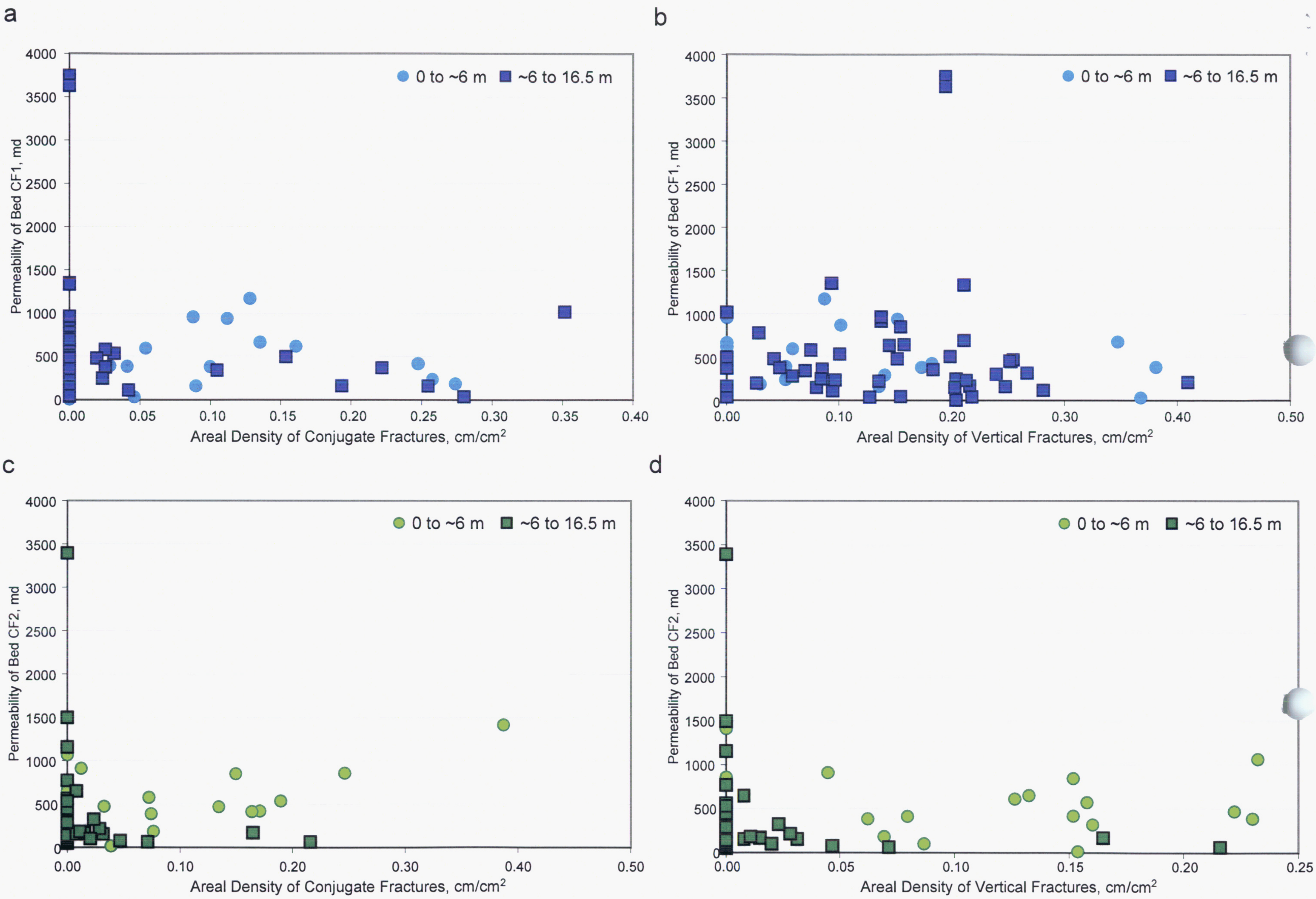

Fig. 14. Crossplots of permeability and areal fracture density illustrate the general absence of direct correlation between these measured properties. (a) Crossplot for Bed CF1 and conjugate fractures with data split into two bins on the basis of faulting intensity. (b) Crossplot for Bed CF1 and vertical fractures. (c) Crossplot for Bed CF2 and conjugate fractures. An intensely faulted zone between 0 and ~6 m along the transect shows a slight correlation with permeability and ~20% of the observed variation in this zone is explained by a linear regression. (d) Crossplot for Bed CF2 and vertical fractures.